

Skyrme-Hartree-Fock-Bogoliubov mass models on a 3D Mesh: Effect of triaxial shape

Guillaume Scamps^{a,1}, Stephane Goriely¹, Erik Olsen¹, Michael Bender²,
Wouter Ryssens^{1,3}

¹Institut d'Astronomie et d'Astrophysique, Université Libre de Bruxelles, Campus de la Plaine CP 226, 1050 Brussels, Belgium

²Université de Lyon, Université Claude Bernard Lyon 1, CNRS, IP2I Lyon / IN2P3, UMR 5822, F-69622, Villeurbanne, France

³Center for Theoretical Physics, Sloane Physics Laboratory, Yale University, New Haven, Connecticut 06520, USA

the date of receipt and acceptance should be inserted later

Abstract The modeling of nuclear reactions and radioactive decays in astrophysical or earth-based conditions requires detailed knowledge of the masses of essentially all nuclei. Microscopic mass models based on nuclear energy density functionals (EDFs) can be descriptive and used to provide this information. The concept of intrinsic symmetry breaking is central to the predictive power of EDF approaches, yet is generally not exploited to the utmost by mass models because of the computational demands of adjusting up to about two dozen parameters to thousands of nuclear masses. We report on a first step to bridge the gap between what is presently feasible for studies of individual nuclei and large-scale models: we present a new Skyrme-EDF-based model that was adjusted using a three-dimensional coordinate-space representation, for the first time allowing for both axial and triaxial deformations during the adjustment process. To compensate for the substantial increase in computational cost brought by the latter, we have employed a committee of multilayer neural networks to model the objective function in parameter space and guide us towards the overall best fit. The resulting mass model BSkG1 is computed with the EDF model independently of the neural network. It yields a root mean square (rms) deviation on the 2457 known masses of 741 keV and an rms deviation on the 884 measured charge radii of 0.024 fm.

1 Introduction

The study of nuclear structure properties enters all chapters of nuclear physics and plays a key role not only

in our understanding of fundamental nuclear theory but also in nuclear applications, such as astronuclear physics [1]. In particular, the properties of atomic nuclei directly impact the description of nuclear reactions which often concern exotic species for which no experimental data exist. Despite significant efforts over several decades, experimental information only covers a fraction of the entire data set required for nuclear applications. Neutron-rich nuclei are of particular interest, especially for understanding how heavy elements are made through the rapid neutron capture process, or r-process, [1,2] and for exploring the limits of nuclear stability [3–5]. A major challenge for nuclear theory is to make reliable extrapolations into regions beyond current experimental reach. To make such predictions, models should strive to (i) contain as many physical ingredients as feasible and (ii) reproduce as accurately as possible known experimental data on relevant observables. The tool of choice for this endeavor is nuclear Density Functional Theory (DFT) [6], the key ingredient of which is the nuclear energy density functional (EDF), which represents an effective interaction based on one-body densities and currents [7–13]. This tool allows for predictions across the entire nuclear chart, firmly founded on a microscopic description of the nucleus.

Particularly important for applications is the *global* reproduction of nuclear masses. The HFB-series based on the Brussels-Montréal (BSk) interactions¹ [11,12,14,15] have demonstrated that a high accuracy on the

^ae-mail: guillaume.scamps@ulb.be

¹Note the nomenclature of the mass model and the Skyrme interaction: each HFB- n mass model is associated with a Skyrme interaction BSk n . For the model we present here, we use the acronym BSkG1 to refer to both the mass model and the Skyrme interaction.

known masses (*i.e.* typically with a root mean square (rms) deviation lower than 0.7 MeV) can be combined with a global description of other properties of finite nuclei (radii, densities, fission barriers, ...) and properties of infinite matter as predicted by ab-initio calculations. Aside from nuclear charge radii and infinite nuclear matter properties, the adjustment protocol of these interactions includes all known atomic masses [16, 17]. Their inclusion is central to the success of these interactions but also renders the construction of new global models extremely demanding.

Depending on the nature of the observables and the types of nuclei considered, adjustments for even a limited number of systems can be extremely computationally demanding. Out of necessity, nuclear configurations considered during adjustment are typically highly restricted, both by the symmetries imposed on them and the choices made to represent them numerically. Such limitations impact both the generality and the numerical precision of the resulting model and do not reflect state-of-the-art EDF calculations, which can now routinely be carried out in large variational spaces with little to no symmetry restrictions [18, 19] for a few nuclei at a time.

For the BSk models, the adjustment procedure relied on (i) the imposition of axial symmetry and (ii) a numerical representation of the single-particle wavefunctions through an expansion in a limited number of harmonic oscillator states (at least in the deformed case) [14, 12, 15, 11]. We present here a new mass model, BSkG1, that is free of these limitations while achieving a comparable accuracy on all known nuclear masses. First, we have moved to a three-dimensional representation that allows us to include, for the first time, triaxial deformations during the adjustment procedure. Second, we have adopted a coordinate-space representation in terms of a Lagrange mesh [20], which presents the advantage of excellent convergence in terms of the basis size [21, 22]. Some applications also require a coordinate-space representation, such as the description of fission processes by time-dependent mean-field methods [23, 24] or of the nuclear pasta phases in neutron star (NS) crusts or core-collapse supernovae [25–28].

Moving from a two-dimensional to a three-dimensional representation comes at a steep computational cost. A typical Skyrme-Hartree-Fock-Bogoliubov calculation for a nucleus, on a laptop, is of the order of a few seconds for a two-dimensional calculation, as opposed to several minutes for a three-dimensional one. To mitigate this, we have developed a new optimization procedure that is well suited to adjust large numbers of parameters to large data sets, employing machine learning tools

inspired by Refs. [29, 30]. Such techniques are becoming ubiquitous in nuclear physics [30–38].

The paper is organized as follows. In Sec. 2, we present the framework of the mass model. In Sec. 3, a new method to adjust the parameters using machine learning techniques is proposed. The results of the BSkG1 mass model are discussed in Sec. 4. Our conclusions and outlook are presented in Sec. 5.

2 Ingredients of the mass model

2.1 The nuclear binding energy

The mass model discussed here, like the BSk models before, describes the atomic nucleus by means of an auxiliary Hartree-Fock-Bogoliubov (HFB) many-body state $|\Phi\rangle$. For any such auxiliary state, we define the total binding energy E_{tot} of a nucleus as follows:

$$E_{\text{tot}}(|\Phi\rangle) = E_{\text{HFB}} + E_{\text{corr}}, \quad (1)$$

where we refer to E_{HFB} as the self-consistent mean-field HFB energy and E_{corr} is a set of perturbative corrections. The distinction between both terms will be discussed in Sec. 2.2.4. The mean-field energy is composed of five terms:

$$E_{\text{HFB}} = E_{\text{kin}} + E_{\text{Sk}} + E_{\text{pair}} + E_{\text{Coul}} + E_{\text{cm}}^{(1)}, \quad (2)$$

which are, respectively, the contributions of the kinetic energy, the Skyrme effective interaction [39–44], a zero-range pairing interaction with appropriate cutoffs [45], the Coulomb force [46, 47], and the one-body part of the centre-of-mass correction. The correction energy E_{corr} consists of three parts:

$$E_{\text{corr}} = E_{\text{rot}} + E_{\text{cm}}^{(2)} + E_{\text{W}}, \quad (3)$$

which are, respectively, the rotational correction [48–50], the two-body part of the centre-of-mass correction [51], and the Wigner energy [52]. In what follows, we will describe each term in more detail separately, but we emphasize here that all of the ingredients of these terms are calculated consistently from the auxiliary state $|\Phi\rangle$.

2.1.1 The Skyrme energy

The total Skyrme energy can be written in terms of an integral over an energy density $\mathcal{E}_t(\mathbf{r})$, where $t = 0, 1$ is the isospin index, as

$$E_{\text{Sk}} = \int d^3\mathbf{r} \sum_{t=0,1} \mathcal{E}_t(\mathbf{r}). \quad (4)$$

The energy density is given by

$$\begin{aligned} \mathcal{E}_t(\mathbf{r}) = & C_t^{\rho\rho} \rho_t^2(\mathbf{r}) + C_t^{\rho\rho\rho'} \rho_0^\gamma(\mathbf{r}) \rho_t^2(\mathbf{r}) \\ & + C_t^{\rho\tau} \rho_t(\mathbf{r}) \tau_t(\mathbf{r}) + C_t^{\rho\Delta\rho} \rho_t(\mathbf{r}) \Delta\rho_t(\mathbf{r}) \\ & + C_t^{\rho\nabla\cdot\mathbf{J}} \rho_t(\mathbf{r}) \nabla \cdot \mathbf{J}_t(\mathbf{r}), \end{aligned} \quad (5)$$

in terms of three local, time-even densities $\rho_t(\mathbf{r})$, $\tau_t(\mathbf{r})$ and $\mathbf{J}_t(\mathbf{r})$ that characterize the auxiliary state $|\Phi\rangle$ [53]. The ten coupling constants $\{C\}$ are determined in terms of the model parameters t_{0-3} , x_{0-3} , W_0 , and W'_0 (see Appendix A for more details).

The functional form of Eq. (5) is closely related (but not equivalent) to the form generated by a (density-dependent) Skyrme effective interaction, and is fairly standard in that respect. Nevertheless, we consider three aspects of Eq. (5) worthy of discussion. First, we employ an extended spin-orbit term as originally introduced in Refs. [40,41] resulting in the presence of two spin-orbit parameters W_0 and W'_0 instead of just one with $W_0 = W'_0$ as was done for the majority of Skyrme EDF parameterizations. Other examples using this extended form are the series of UNEDF interactions [10, 42,44] and those of Ref. [7]. Second, as with the BSk forces after BSk19 [11,15,52], SLy4 [43], SkM* [39], UNEDF0 [42] and UNEDF1 [44], Eq. (5) does not include the terms bilinear in the spin-current tensor density $J_{\mu\nu}(\mathbf{r})$ that are obtained when evaluating the expectation value of an effective two-body Skyrme interaction [53]. Third, we do not consider any terms involving time-odd densities for finite nuclei, as all such contributions vanish identically for the configurations we consider during the model adjustment, see Sec. 2.2.2.

2.1.2 The pairing energy

To incorporate the effect of pairing correlations, we include a simple pairing term of the form

$$E_{\text{pair}} = \sum_{q=p,n} \frac{V_{\pi q}}{4} \int d^3\mathbf{r} \left[1 - \eta \left(\frac{\rho_0(\mathbf{r})}{\rho_{\text{sat}}} \right)^\alpha \right] \tilde{\rho}_q^*(\mathbf{r}) \tilde{\rho}_q(\mathbf{r}), \quad (6)$$

where $\rho_{\text{sat}} = 0.16 \text{ fm}^{-3}$ and $\tilde{\rho}_q(\mathbf{r})$ is the local pairing density [54]. The parameter η changes the character of the pairing interaction from being mainly active in the nuclear volume ($\eta = 0$) to being limited to the nuclear surface region ($\eta = 1$).

The contribution of each individual single-particle state to the pairing density $\tilde{\rho}_q(\mathbf{r})$ is weighted with a cutoff factor $f_{q,i}^{\text{pair}}$, limiting the pairing interaction to levels in an energy window around the Fermi energy λ_q . These factors take the form [45]

$$f_{q,i}^{\text{pair}} = \prod_{\sigma=\pm 1} \left[1 + e^{\sigma(\epsilon_i - \lambda_q - \sigma E_{\text{cut}})/\mu_{\text{pair}}} \right]^{-1/4}, \quad (7)$$

where ϵ_i is the single-particle energy of the i -th single-particle state in the basis that diagonalizes the single-particle Hamiltonian, $\mu_{\text{pair}} = 0.5 \text{ MeV}$ and E_{cut} is the energy cut-off, which is an adjustable parameter of the model.

2.1.3 The Coulomb energy

We only take into account the direct contribution of the Coulomb interaction to the energy

$$E_{\text{Coul}} \equiv E_{\text{Coul}}^{\text{direct}} = \int d^3\mathbf{r} U(\mathbf{r}) \rho_c(\mathbf{r}), \quad (8)$$

where $\rho_c(\mathbf{r})$ is the charge density of the nucleus. $U(\mathbf{r})$ is the Coulomb potential satisfying the electrostatic Poisson equation for the charge density $\rho_c(\mathbf{r})$

$$\Delta U(\mathbf{r}) = -4\pi e^2 \rho_c(\mathbf{r}), \quad (9)$$

with e^2 the square of the elementary charge. To account for the finite size of the charge distributions of individual protons and neutrons, the charge density in Eqs. (8) and (9) is constructed through the folding of (point) proton and neutron densities with appropriate form factors. For protons, we employ the Gaussian form factor of Ref. [55], characterized by the rms radius of the proton $r_p = 0.895 \text{ fm}$ of Ref. [56]. For neutrons, we employ the difference of two Gaussians of widths $r_+^2 = 0.387 \text{ fm}^2$ and $r_-^2 = 0.467 \text{ fm}^2$ [57], corresponding to a neutron mean square charge radius of -0.116 fm^2 .

As a practical recipe to simulate beyond mean-field Coulomb correlations, we drop the exchange contribution of the electrostatic interaction entirely. This recipe was first studied in Ref. [46], and employed in the HFB-series of mass models, starting with HFB-15 [47].

2.1.4 The Wigner energy

The Wigner energy is a phenomenological term included to simulate the excess binding energy of $N \sim Z$ nuclei. We take the form introduced in Ref. [52]:

$$\begin{aligned} E_W = & V_W \exp(-\lambda((N-Z)/A)^2) \\ & + V'_W |N-Z| \exp[-(A/A_0)^2], \end{aligned} \quad (10)$$

which depends on four parameters V_W , V'_W , λ , and A_0 . This correction chiefly influences light and $N \simeq Z$ nuclei.

2.1.5 Centre-of-mass correction

Although the details vary, the inclusion of some correction for spurious motion of the centre-of-mass of the nucleus is standard practice in the literature [6]. This correction reads

$$E_{\text{cm}} = -\frac{1}{2mA} \langle \hat{\mathbf{P}}_{\text{cm}}^2 \rangle \equiv E_{\text{cm}}^{(1)} + E_{\text{cm}}^{(2)}, \quad (11)$$

where m is the (average) nucleon mass and A is the mass number. We split this correction into two separate contributions. The one-body part can be taken into account as a rescaling of the kinetic energy [6], but the calculation of the two-body contribution is much more complicated, as described in Ref. [51].

2.1.6 The rotational correction

Less standard in the literature is the inclusion of a rotational correction, whose goal is to simulate the effect of the restoration of rotational symmetry. Inspired by the HFB mass models of Ref. [11] and references therein, we employ a correction based on a simple perturbative cranking model, involving the Belyaev moments of inertia (MOI) around the three principal axes of the nucleus, \mathcal{I}_μ ($\mu = x, y, z$) [48, 53]:

$$E_{\text{rot}} = - \sum_{\mu=x,y,z} f_\mu^{\text{rot}} \frac{\langle \hat{J}_\mu^2 \rangle}{2\mathcal{I}_\mu}, \quad (12a)$$

$$f_\mu^{\text{rot}} = b \tanh \left(c \frac{\mathcal{I}_\mu}{\mathcal{I}_c} \right), \quad (12b)$$

where \hat{J}_μ is an angular momentum operator and $\mathcal{I}_c = \frac{2}{15} m R^2 A$ is (one third of) the MOI of a rigid rotor of radius $R = 1.2A^{1/3}$, comprised of A nucleons of average mass $m = \frac{1}{2}(m_n + m_p)$. The three MOI in Eq. (12a) are obtained consistently from the auxiliary state $|\Phi\rangle$, but their calculation is not trivial, and we refer to Appendix B for a more detailed discussion.

The inclusion of a cutoff factor f_μ^{rot} in Eq. (12a) is necessary to smooth the transition between deformed and spherical nuclei. In early tests, we employed the smoothing prescription of Refs. [49, 50], but found it unsuitable for triaxial systems. Although they are of similar size, our parameters b and c are therefore not directly comparable to their counterparts in Refs. [49, 50].

2.2 Self-consistent HFB calculations in coordinate-space

2.2.1 Coordinate-space representation: the MOCCa code

The variation of the mean-field energy E_{HFB} leads to the self-consistent Skyrme-HFB equations, which need to be solved iteratively [53, 58]. To this end, we employ the MOCCa code [59–61], which represents the single-particle wave functions on a three-dimensional Cartesian Lagrange mesh [20, 62–64, 53]. This representation allows us to treat different nuclear shapes on an equal footing and yields a high numerical accuracy that is essentially independent of deformation [21].

The MOCCa code is similar in spirit to the earlier EV8 code [63, 53], but differs from it in four respects. First, MOCCa allows the user significant freedom of choice with respect to self-consistent symmetries and is capable of completely symmetry-unrestricted calculations. Second, it further improves on the numerical accuracy of EV8 through the self-consistent use of Lagrange derivatives instead of employing finite difference formulas on the mesh [21]. Third, MOCCa's further algorithmic improvements have made its iterative process faster than EV8's by up to an order of magnitude [61]. Finally, MOCCa is equipped to handle pairing correlations at the HFB level, employing the two-basis method [62, 61].

Throughout the adjustment process, we employed cubic meshes with $N_x = N_y = N_z = 32$ points and a mesh spacing $dx = 0.8$ fm. During the final calculation, we expanded the lattice to $N_x = N_y = N_z = 36$. With these numerical choices, we can estimate that the calculated binding energies and rms radii will not change by more than a few tens of keV and 0.01 fm respectively for the majority of nuclei when further expanding the numerical basis [21]. Achieving comparable accuracy using basis-expansion methods requires the inclusion of a number of harmonic oscillator states that is prohibitive for calculations on the scale of the nuclear chart, for both Skyrme [65] and Gogny EDFs [22].

To avoid the extreme memory requirements of representing a complete set of single-particle states on coordinate meshes of this size, we store and iterate only the N_N neutron states and N_Z proton states with lowest single-particle energy. On the order of a few hundred single-particle states suffices to calculate all relevant quantities, which are all computed from the single-particle states weighted by their occupation numbers². For a given nucleus, we iterated $N_N = N + 160$ neutron and $N_Z = Z + 100$ proton states during the adjustment

²With the exception of the Belyaev MOI, see Appendix B.

process. For the final calculation of the mass table we increased these numbers to $N_N = N + 400$ neutron and $N_Z = Z + 240$ proton states.

Previous BSk models were adjusted using an implementation that relied on an expansion of the single-particle wave functions in a set of harmonic oscillator basis states. An important difference between this type of numerical representation and a coordinate space one is the treatment of pairing. First, the discretization of the continuum of both approaches is vastly different, resulting in a different spectrum of positive-energy single-particle states. Second, the limited number of single-particle states we iterate forces us to limit the width of the pairing window, resulting in values of E_{cut} in Eq. (7) that are significantly smaller than those typically used in harmonic oscillator approaches. The combination of these differences makes it essentially impossible to directly use the BSk functionals in our coordinate space representation, and clearly indicates the need for a new fit.

2.2.2 Imposed symmetries: nuclear configurations considered

EDF-based nuclear models rely on the notion of intrinsic symmetry breaking to achieve their descriptive power. It is in principle desirable to perform completely symmetry-unrestricted calculations, *i.e.* to consider the most general nuclear configurations without any restrictions. Although the MOCCa code can perform such symmetry-unrestricted calculations, those come at a price: (i) they significantly increase the computational cost and (ii) they imply the loss of all quantum numbers, making interpretation of results and comparison to experiments difficult. Techniques to restore broken symmetries and recover the associated quantum numbers for triaxial configurations exist [66], but are beyond the scope of this contribution.

In fact, there is a large body of empirical evidence that the HFB ground states of all nuclei usually adopt one or several spatial symmetries, which can be used to simplify the numerical treatment by imposing those that remain conserved for most, if not all, nuclei. We have restricted ourselves here to nuclear configurations that respect three plane-reflection symmetries, as well as time-reversal symmetry. This choice of spatial symmetries results in nuclear shapes that are reflection-symmetric and are invariant under discrete rotations of 180° around any principal axis. If visualized, virtually all configurations discussed here would resemble ellipsoids with three principal axes of (possibly) different lengths. This resemblance is not exact, and large numbers of nuclei exploit non-zero values of higher-order

multipole deformations beyond quadrupole, as will be discussed below.

A nucleus with non-axial deformation does not exhibit any continuous rotational symmetry, and we consequently cannot assign any definite rotational quantum number. The only non-trivial quantum number we can assign without ambiguity for all configurations considered is parity. Eliminating this restriction would allow us to study reflection asymmetric nuclear configurations, which are typically characterized by a non-zero octupole deformation. Such configurations are of importance for the description of fission barriers [49, 67], but systematic calculations have shown that static octupole deformation is only expected for a limited number of nuclides [68–70]. While the effect on the binding energy for these isotopes can be sizeable (up to 2 MeV), we have opted to not explore octupole deformation for this study. Imposing time-reversal symmetry on the other hand chiefly limits our description of odd- A and odd-odd nuclei, which we will discuss in more detail in the next section. But it can already be noted here, however, that the contribution from these terms to the total binding energy remains on the order of at most a few hundred keV [71, 72] and thereby remains smaller than the average deviation of nuclear masses that we achieve in the parameter adjustment.

Lifting the restrictions imposed by reflection symmetry and time-reversal invariance is feasible, and the necessary preparations for doing so in future mass fits are underway. We note that the expected increase in complexity due to these generalizations is significantly smaller than the one incurred when generalizing from two-dimensional axially-symmetric shapes to three-dimensional triaxial shapes, as we explore here.

The shape of the nuclear density can be characterized in terms of multipole moments $\hat{Q}_{\ell m} \equiv \hat{r}^\ell \hat{Y}_{\ell m}$, where $\hat{Y}_{\ell m}$ is a spherical harmonic. With the symmetries chosen here, all multipole moments $\langle \hat{Q}_{\ell m} \rangle$ are real, and can take finite values only when ℓ and m are both even. The multipole moments are most transparently discussed in terms of dimensionless deformation parameters $\beta_{\ell m}$, which we define as

$$\beta_{\ell m} = \Re \left(\frac{4\pi}{3(r_0 A^{1/3})^\ell A} \langle \hat{Q}_{\ell m} \rangle \right), \quad (13)$$

where $r_0 = 1.2$ fm. We emphasize that these multipole moments characterize the shape of the nuclear *volume*, rather than the deformation of the nuclear *surface*. The latter type of moments is generally employed in microscopic-macroscopic approaches, such as the ϵ_ℓ defined in Ref [73].

For states obtained from a self-consistent minimization it is not unusual to find numerically significant mul-

tipolarities as large as $\ell = 10$, but we will mainly discuss the quadrupole ($\ell = 2$) moments, $\langle \hat{Q}_{20} \rangle$ and $\langle \hat{Q}_{22} \rangle$ as they represent the dominant deformation modes. The nuclear quadrupole deformation is also often discussed in terms of the total size of the deformation β and the triaxiality angle γ :

$$\beta = \sqrt{\beta_{20}^2 + 2\beta_{22}^2}, \quad (14a)$$

$$\gamma = \text{atan}\left(\sqrt{2}\beta_{22}/\beta_{20}\right). \quad (14b)$$

With the symmetries imposed on our calculations, we can limit the discussion to one sextant of the β - γ plane. For finite values of β , prolate shapes correspond to $\gamma = 0^\circ$ while oblate shapes correspond to $\gamma = 60^\circ$. The introduction of the triaxial degree of freedom allows the nucleus to explore all values of γ in between these two extremes.

The size of the quadrupole deformation, β , is a rotational invariant. For higher order multipole deformations, we can similarly define rotational invariants β_ℓ as

$$\beta_\ell = \sqrt{\sum_{m=-\ell}^{\ell} \beta_{\ell m}^2}. \quad (15)$$

The value of β_ℓ does not specify completely the deformation of the nucleus at order ℓ , and only for $\ell = 2$ does the value of the single additional quantity (γ) suffice to do so.

From a practical point of view, the three conserved spatial symmetries allow us to limit the calculations to a mesh of effective dimensions ($N_x/2, N_y/2, N_z/2$) while we can exploit time-reversal to limit the effective calculation to $N_N/2$ and $N_Z/2$ single-particle states [53], reducing the computational burden in both CPU time and memory required by a factor of eight compared to the most general possible calculation.

2.2.3 Nuclei with odd nucleon number(s)

The fully self-consistent treatment of odd- A and odd-odd nuclei in the context of HFB theory requires the construction of one or two quasiparticle excitations with respect to a reference state of even-even character. Because of polarization effects, this blocking procedure results in an auxiliary HFB state that is no longer invariant under time-reversal, which in turn implies the need to consider terms involving time-odd densities in the Skyrme EDF [6].

As we focus in this study on the impact of non-axial shapes and using a coordinate-space representation, we

opted to side-step this complexity, employing the equal-filling method [74] to construct statistical mixtures of Bogoliubov reference states that are manifestly time-reversal invariant. This approximation takes into account the blocking effect due to the odd nucleon(s), but neglects polarization effects due to time-odd terms of the EDF.

The blocking of quasiparticles can render self-consistent HFB calculations notoriously difficult to converge [71]. The chief reason for this is the need to select, at every self-consistent iteration, the appropriate quasiparticle(s) to block. This procedure is to a certain degree robust, if one targets states that are characterized by a set of quantum numbers or, more generally, by fixed expectation values of one or more operators. In our case, however, we are interested in the overall lowest binding energy *after self-consistency is achieved*, independent of the characteristics of the auxiliary HFB state.

Our strategy consists of blocking the quasiparticle with the lowest quasiparticle energy at every iteration. Nevertheless, from any given iteration to the next, the candidate quasiparticle excitation can change dramatically in character. To limit somewhat the destructive influence of crossings in the quasiparticle energies, we employ parity as the sole remaining quantum number. For an odd- A nucleus we thus perform two calculations, constructing both the lowest blocked states of positive and negative parity. For an odd-odd nucleus, we perform four calculations to construct all possible combinations of one-proton-one-neutron excitations for a given parity of each species that are lowest in energy. The parity corresponding to the lowest overall energy is taken as that of the ground state. While computationally costly, this strategy results in at least one converged calculation for virtually all nuclei throughout the adjustment.

Finally, a comment on the angular momentum quantum number J is in order. The quantum numbers J^π of the ground states of odd- A and odd-odd nuclei are of great interest, but, as mentioned above, we can only assign the parity quantum number π . We have made no effort to extract any predictions for J from our calculations due to the lack of rotational quantum numbers. In principle, one could employ a simple model to extract J from a symmetry-broken mean-field calculation, such as a strong-coupling model in the case of an axially deformed configuration. However, this type of argument is generally only applicable in limited regions of the nuclear chart (usually heavy, well-deformed and axially symmetric nuclei). We are not aware of any recipe that is globally applicable, except for the extremely demanding symmetry restoration techniques that are beyond the scope of the present global study.

2.2.4 Minimization of the energy

Ideally, one would like to employ the variational principle and minimize the total energy (Eq. 1). The formal variation of E_{HFB} is rather straightforward, and numerical minimizations of this quantity are performed routinely nowadays. The self-consistent equations become significantly more involved if the two-body centre-of-mass and rotational corrections are included in the optimization. The variation of $E_{\text{cm}}^{(2)}$ has only rarely been performed consistently, exceptions being the SLy6 and SLy7 parameterizations of Ref. [43]. To the best of our knowledge, the consistent variation of the rotational correction E_{rot} has never been attempted.

Traditionally, if a two-body centre-of-mass correction or a rotational correction are included in the model, they are treated *perturbatively*: one calculates the total energy $E_{\text{tot}}(|\Phi_0\rangle)$ from the auxiliary state $|\Phi_0\rangle$ which minimizes the mean-field energy E_{HFB} only. While easy to implement, a perturbative approach suffers greatly if two (or more) coexisting auxiliary states have a quasi-identical mean-field energy E_{HFB} but different E_{corr} . In such cases, a perturbative approach will result in disproportionately large changes in the total energy E_{tot} when either varying the nucleon number or (slightly) varying the parameters of the Skyrme interaction, leading respectively to unphysical separation energies or convergence problems for the fitting procedure.

Instead of a perturbative treatment, we have employed a *semivariational* strategy to include these corrections. For a given nucleus, we perform a large number of calculations that include $E_{\text{cm}}^{(2)}$ and E_{rot} perturbatively, each constrained to different values of the quadrupole deformation. Our final value for the binding energy is then selected as the overall minimum of the total energy E_{tot} as a function of quadrupole deformations with a resolution of $\Delta\beta_{20} = \Delta\beta_{22} = 0.005$. We emphasize that we also employ this strategy for blocked calculations: we scan the full β - γ -plane for each type of quasiparticle excitations considered, resulting in two scans for odd- A and four scans for odd-odd nuclei.

Despite the evident computational complexity of this approach, we have adopted the semivariational strategy for three reasons. First and foremost, early tests showed a systematically improved description of the binding energies. Second, the inclusion of quadrupole constraints increases the stability of blocked calculations by limiting the amount of possible single-particle level crossings in any single calculation (see also the previous section). Finally, this approach greatly alleviates the problem associated with coexisting mean-field minima discussed above.

3 Model adjustment using neural networks

Our mass model depends on 22 parameters: eleven are related to the Skyrme EDF ($t_0, t_1, t_2, t_3, x_0, x_1, x_2, x_3, W_0, W'_0, \gamma$), five to the zero-range pairing interaction ($V_{\pi n}, V_{\pi p}, E_{\text{cut}}, \eta, \alpha$), two to the rotational correction (b, c), and four to the Wigner energy (V_W, λ, V'_W, A_0). During the fitting procedure, we set $\gamma = 0.3$ to ensure the correct description of the nuclear matter incompressibility and impose a symmetry energy at saturation density of $J = 32$ MeV to ensure a minimal stiffness of the neutron matter equation of state [11].

Referring to the parameters as $\boldsymbol{\chi} = (t_0, t_1, \dots)$, our goal is to minimize an objective function $\sigma_{\text{rms}}(\boldsymbol{\chi})$, defined for several observables O as

$$\sigma_{\text{rms}}(\boldsymbol{\chi}) = \sqrt{\sum_{N,Z,O} [W_O \sigma(N, Z, \boldsymbol{\chi}, O)]^2}, \quad (16)$$

in terms of weights W_O for each observable and the deviations between experimental and calculated values $\sigma(N, Z, \boldsymbol{\chi}, O) = O_{\text{exp}}(N, Z) - O_{\text{th}}(N, Z, \boldsymbol{\chi})$. The objective function considered here includes all the 2408 binding energies known experimentally for $Z, N \geq 8$ nuclei [16], making even a single evaluation of Eq. (16) a demanding task.

In principle, we could proceed to minimize the objective function using traditional minimization methods. However, any systematic search of the high-dimensional parameter space is prohibitively expensive. The problem is further complicated by the nonlinearity of the self-consistent Skyrme-HFB equations: it is not easy to predict the results of even small variations of individual parameters.

In order to explore the parameter space efficiently, we have developed a new approach inspired by Ref. [30]. We consider a committee of Multi-Layer Neural Networks (MLNNs) [75] as an emulator, *i.e.* as a computationally cheap estimate of the observables as a function of N, Z and $\boldsymbol{\chi}$. Each individual MLNN aims to provide an estimate for the output of the code, *i.e.* an estimate $\sigma'(N, Z, \boldsymbol{\chi}, O)$ of the actual $\sigma(N, Z, \boldsymbol{\chi}, O)$. The minimum of the estimated objective function $\sigma'(\boldsymbol{\chi})$ can be found at little computational cost, resulting in a prediction for an optimal parameter set by each member of the committee. Until convergence of the value of the objective function, the MLNNs are trained on an increasing set of MOCCa calculations in regions of the parameter space deemed promising by the committee.

During the optimization procedure, our committee typically consists of $N_{\text{NN}} = 300$ neural networks. Each individual member consists of four hidden layers of neu-

ron number³ 128, 64, 32, and 16. The output layer aims at estimating the difference between theoretical and experimental values for a given observable, based on the values of N , Z and χ . To aid the learning process, we provide each member with additional information: the mass number A , the number parity of both N and Z , the distance to the closest magic number (up to 126) and individual terms of the liquid drop model for the nuclear binding energy ($A^{2/3}$, $Z(Z-1)/A^{1/3}$, $(N-Z)^2/A$, and $A^{-1/2}$).

Every MLNN is initialized randomly and trained on available data obtained from MOCCa calculations (see below) using the Keras/Tensorflow libraries [75]. Once trained, we minimize the objective function (as modelled by each member of the committee) with respect to the mass model parameters using the trust region reflective algorithm [76]. This results in a predicted optimal parameter set χ^i , one for each member of the committee ($i = 1, \dots, N_{\text{NN}}$). As each member is initialized differently, they will provide slightly different predictions and so propose different candidate parameter sets.

The MLNNs are trained on an always-increasing library of MOCCa calculations, *i.e.* an individual data point is the difference between the experimental value of an observable and the calculated value for a given nucleus and a value of χ . To start the learning procedure, we compute a first set of $N_{\text{ini}} \sim 1000$ such data points, for essentially random nuclei within the AME2016 database with $Z \geq 8$, and $N \geq 8$ and values of the mass model parameters in a given range. When possible these limits are taken from constraints imposed on nuclear matter properties [52,11] and obtained by reasonable guess otherwise.

After the initial training, we keep growing the training library guided by the predictions of individual committee members. For each candidate parameter set χ^i , we calculate observables for three random nuclei, resulting in $3N_{\text{NN}}$ extra data points. Continuing the data set training on the expanded data set, we generate new candidate parameter sets. This process is continued until convergence, *i.e.* until we achieve no significant further decrease of the objective function.

Periodically, we interrupt this individual phase of the optimization strategy to include either (i) a collective decision of the committee or (ii) an active learning step. Every time the data set is increased by $N_{\text{coll}} \sim 8000$ data points, we perform a collective step. When the data set is increased by a further $N_{\text{act}} \sim 4000$ points, we perform an active learning step.

³All the neurons have a rectifier activation function $f(x) = \max(0, x)$.

A collective step is started by polling every member of the committee on the candidate parameter sets of *the other members*. Every candidate parameter set is then assigned a collective estimated deviation $\sigma_{\text{rms}}^{\text{coll}}(\chi^i)$, computed as the 9th decile of the modelled deviations for this parameter set among all members of the committee.⁴ Among the N_{NN} candidate parameter sets, we select the one with the lowest collectively-estimated deviation and use it to perform MOCCa calculations for all nuclei (*i.e.* 2408 data points). Once these results are added to the data set, the individual training phase resumes.

In an active learning step, we identify 100 pairs of nuclei and parameters sets whose predicted contribution to the objective function is the largest for every candidate parameter set χ^i . We perform MOCCa calculations for this set of nuclei-interaction pairs, thereby generating data that is likely to improve the overall predictions of the committee members.

We note that the Wigner energy E_W was not included in the machine-learning protocol. Since it is a simple analytical function of N , Z and the four parameters (V_W, V'_W, λ, A_0), we have simply added it manually to the output of each MLNN. This reduces the difficulty of the learning, as the committee members do not need to know the dependence of the results on these parameters.

After convergence we performed a full calculation for all nuclei with $8 \leq Z \leq 110$ from the proton- to the neutron-drip line using the final parameter set. All the results presented below are generated with the MOCCa code, none of them are predictions by a neural network.

4 The BSkG1 parameterization

4.1 Ingredients of the objective function and parameter values

As mentioned above, the objective function (Eq. 16) includes all the 2408 measured masses for Z , $N \geq 8$ nuclei compiled with the 2016 atomic mass evaluation (AME2016) database [16]. However, it is well known that fits based solely on nuclear masses generally lead to an excessive pairing strength [77], hence to unreliable extrapolations towards unknown regions of the nuclear chart. To avoid such a shortcoming, it is important to either constrain the pairing strength or include additional observables in the objective function. To that aim, we added to the objective function the

⁴One could imagine more straightforward recipes to assign a collective score, such as the average of all modelled deviations, but we have found these to be not very reliable in early tests.

Table 1 BSkG1 parameter set: 16 parameters characterizing the self-consistent mean-field energy E_{HFB} and 6 corresponding to the correction energy E_{corr} .

Parameters	BSkG1
t_0 [MeV fm ³]	-1882.36
t_1 [MeV fm ⁵]	344.79
t_2 [MeV fm ⁵]	-2.43198
t_3 [MeV fm ^{3+3γ}]	12322.0
x_0	0.196276
x_1	-0.580308
$x_2 t_2$ [MeV fm ⁵]	-170.203
x_3	0.120751
W_0 [MeV fm ⁵]	123.922
W'_0 [MeV fm ⁵]	83.519
γ	0.3
$V_{\pi n}$ [MeV]	-644.921
$V_{\pi p}$ [MeV]	-682.559
η	0.692
α	0.77
E_{cut} [MeV]	7.42
b	0.93
c	5.00
V_W [MeV]	-1.905
λ	272.2
V'_W [MeV]	0.671
A_0	36.211

MOI of heavy nuclei deduced from observed rotational bands. This set consists of 48 even-even nuclei, most of which are neutron-rich rare-earth nuclei [78–80]. We compare the experimental values with the calculated Belyaev MOI (see also Appendix B), which are highly sensitive to the strength of the pairing interaction.

Following the Brussels-Montréal protocol, charge radii as well as nuclear matter properties are also qualitatively included in the fitting strategy, though they are not explicitly included in the objective function. This was achieved by constraining some of the nuclear matter properties, as followed in Ref. [11], namely (i) the symmetry coefficient is set to $J = 32$ MeV to ensure a certain degree of stiffness of the infinite neutron-matter equation of state [11]; (ii) the Fermi wave number k_F is determined to best reproduce nuclear charge radii; (iii) the exponent γ is set to 0.3 to ensure the incompressibility K_v of charge-symmetric infinite nuclear matter lies within the interval $230 \leq K_v \leq 250$ MeV [81]; and (iv) the isoscalar effective mass M_s^*/M at the saturation density n_0 is taken close to the value of 0.84, as predicted by extended Brueckner-Hartree-Fock (EBHF) calculations [82, 83].

Our committee-guided adjustment procedure proved particularly practical in exploring the compromise between the reproduction of all nuclear masses and the reproduction of charge radii, realistic pairing, and nu-

clear matter properties. Once the members are sufficiently trained, the committee can propose different parameterizations (and estimate their properties) as a function of the weights W_O at low computational cost. For instance, this allowed us to thoroughly explore the trade-off between masses and MOI by varying the relative weights $W_{\text{MOI}}/W_{\text{mass}}$ without the need to restart the fit multiple times.

We refer to the final functional of the adjustment procedure as BSkG1, the parameters of which are shown in Table 1. The corresponding infinite nuclear matter properties are given in Table 2. The rms σ and mean deviation $\bar{\epsilon} = \overline{O_{\text{exp}}(N, Z) - O_{\text{th}}(N, Z)}$ for both the masses and charge radii are given in Table 3. Note that the model was adjusted to the AME2016 masses [16] leading to an rms deviation of 0.734 MeV with respect to all the 2408 masses. However, the deviations given in Table 3 have been calculated with respect to the (slightly larger) set of masses contained in the recently published AME2020 database [17]. Finally, to render our results completely reproducible, we provide values for the physical constants as they were used during the readjustment: $\frac{\hbar^2}{2m_n} = \frac{\hbar^2}{2m_p} = 20.73553$ MeV fm² and $e^2 = 1.43996446$ MeV fm, where e is the unit of charge.

Table 2 Infinite nuclear matter properties and final rms σ for the BSkG1 parameterization. See Sec. 4.3 and Refs. [11, 84, 85] for the various definitions.

Properties	BSkG1
k_F [fm]	1.3280
n_0 [fm ⁻³]	0.1582
a_v [MeV]	-16.088
J [MeV]	32.0
L [MeV]	51.7
M_s^*/M	0.860
M_v^*/M	0.769
K_v [MeV]	237.8
K_{sym} [MeV]	-156.4
K' [MeV]	376.7
G_0	0.35
G'_0	0.98

4.2 Properties of finite nuclei

4.2.1 Nuclear masses and separation energies

Figure 1 shows the difference between masses calculated with BSkG1 and experimental values as a function of both N and Z . The overall agreement is excellent and only a limited number of nuclei show a deviation of more than 2 MeV. The largest systematic deviations

Table 3 Final rms σ and mean $\bar{\epsilon}$ (exp-theory) deviations with respect to the 2457 known masses M where $Z, N \geq 8$ [17], the 2309 neutron separation energies S_n , the 2173 β -decay energies Q_β , and the 884 measured charge radii R_c [86] for the mass model generated with the BSkG1 parameterization. The first line gives the model error [87] on all the 2457 measured masses. Note that the model was adjusted on the AME2016 database [16], but all deviations here are calculated with respect to the 2020 update AME2020 [17].

Results	BSkG1
$\sigma_{\text{mod}}(M)$ [MeV]	0.734
$\sigma(M)$ [MeV]	0.741
$\bar{\epsilon}(M)$ [MeV]	-0.026
$\sigma(S_n)$ [MeV]	0.466
$\bar{\epsilon}(S_n)$ [MeV]	0.000
$\sigma(Q_\beta)$ [MeV]	0.645
$\bar{\epsilon}(Q_\beta)$ [MeV]	0.000
$\sigma(R_c)$ [fm]	0.0239
$\bar{\epsilon}(R_c)$ [fm]	-0.0008

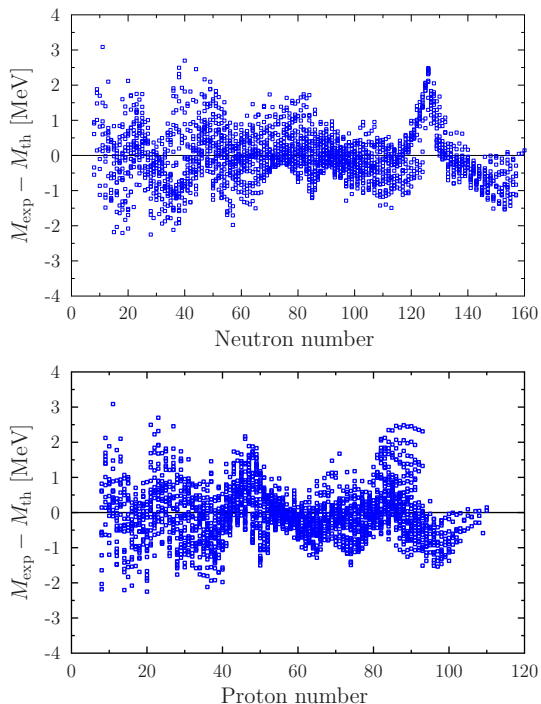


Fig. 1 (Color online) Differences between experimental [17] and theoretical masses as a function of N and Z for BSkG1 (blue squares).

can be seen for the lightest nuclei, and around the $N = 126$ shell closure; smaller deviations can also be seen in the vicinity of other magic numbers.

The new model achieves an rms deviation on the 2457 known AME2020 masses of 0.741 MeV, which is somewhat larger than that achieved by the latest BSk-based HFB mass models [11, 15, 88]. In what follows, we will primarily compare to the HFB-21 [88] and HFB-

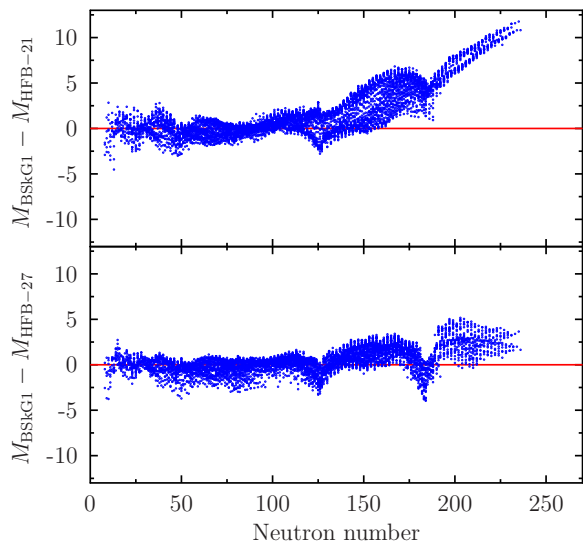


Fig. 2 (Color online) Comparison between the masses predicted with the BSkG1 interaction and HFB-21 (top panel) and HFB-27 (lower panel). All nuclei with $8 \leq Z \leq 110$ lying between the BSkG1 proton and neutron drip lines are included.

27 [15] mass tables, characterized by rms deviations on the nuclear masses of 0.577 and 0.517 MeV on the AME2020 masses, respectively. The latter is based on a Skyrme EDF of standard form, and is quite similar to BSkG1 in many respects, while HFB-21, which has been used extensively to study r-process abundances (see e.g. Refs. [89–91]), incorporates non-standard t_4 and t_5 terms in the Skyrme functional, *i.e.* terms that are simultaneously momentum and density dependent.

Both HFB-21 and HFB-27 achieve an overall lower rms deviation, mainly because of the following three reasons. The first is their lower value of the symmetry coefficient $J = 30$ MeV, which favors the reproduction of masses [52] but would lead in our case to an equation of state for neutron matter of insufficient stiffness. The second is the treatment of the pairing strength: where BSkG1 employs one parameter for each nucleon species, both HFB-21 and HFB-27 employ two different parameters, depending on whether the nucleon number is even or odd; in addition the BSk pairing cut-off parameter around 16 MeV was found to improve the mass accuracy with respect to lower values (as used here), at least if no regularization of the pairing is performed [77]. Third, both HFB-21 and HFB-27 employ a phenomenological correction for collective motion that includes a vibrational component on top of the rotational contribution as adopted here.

Nevertheless, the accuracy of the BSkG1 masses is significantly better than those of popular Skyrme parameterizations such as SLy4 [43] or SLy5s1 [92]. When

evaluated in our framework for the 561 known masses of even-even nuclei, these parameterizations give rise to rms deviations of 3.9 and 8.7 MeV, respectively. The UNEDF collaboration reports rms deviations on the masses of 555 even-even nuclei of 1.428, 1.912 and 1.950 MeV for the UNEDF0, UNEDF1 and UNEDF2 parameterizations, respectively [10]. The D1M mass model, based on the finite-range Gogny interaction [12] gives an rms deviation comparable to that of BSkG1, *i.e.* 0.810 MeV on the latest AME2020 masses.

When dealing with extrapolated masses away from the experimentally known region, the BSkG1 masses may differ in a non-negligible way from those predicted by the BSk-based HFB mass models. In particular, Fig. 2 shows, for all $Z \leq 110$ nuclei lying between the BSkG1 proton and neutron drip lines, the mass differences between the BSkG1 and HFB-21(top panel) or HFB-27 (bottom panel) masses as a function of the neutron number. Large differences are observed with respect to HFB-21, especially for the heavy neutron-rich nuclei beyond $N = 170$. In contrast, BSkG1 masses are found to be rather similar to HFB-27, with differences typically smaller than 5 MeV. For both HFB models, there are, however, significant differences to be seen near $N = 184$, and to a lesser extent $N = 126$, indicating a different description of shell structure, as discussed in more detail below.

As typical examples, we show the two-neutron separation energies S_{2n} for the isotopic chains of Sn, Sm, Pb, and Fm in Fig. 3 for both BSkG1 and HFB-21, as well as the available experimental data. Even though differences for individual nuclei can be large, the general trends for BSkG1 and HFB-21 are comparable and generally reproduce experimental data rather well. The exceptions are the regions around $N = 126$ and $N = 184$, where HFB-21 and BSkG1 each exhibit signs of a different shell structure. Particularly around $N = 126$, HFB-21 offers a better description of experimental data. Those differences can be seen more clearly in Fig. 4, as discussed below.

Since separation energies are differences of binding energies, they are directly impacted by the numerical accuracy of the calculation. Compared to HFB-21, the coordinate space representation used here for BSkG1 results in much smoother separation energies. Irregularities are not totally absent, and can be seen for example near the neutron drip lines for the Sn and Sm isotopes and for neutron-deficient Pb isotopes. Our numerical accuracy in these cases is not limited by the numerical representation, but rather by the resolution of our scan of the β - γ plane (see Sec. 2.2.4).

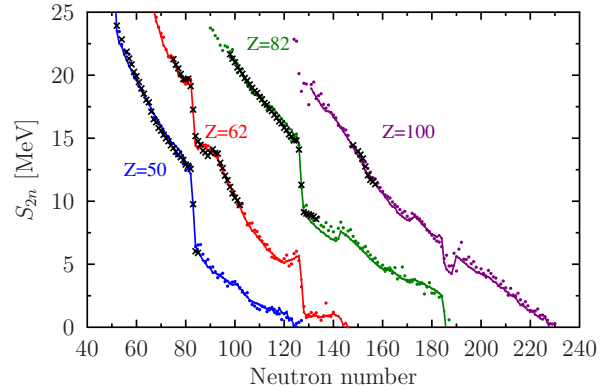


Fig. 3 (Color online) Two-neutron separation energies S_{2n} for the isotopic chains of Sn, Sm, Pb, and Fm as a function of the neutron number, from AME2020 [17] (black crosses) or predicted either by HFB-21 (dots) or BSkG1 (lines) masses.

4.2.2 Shell structure

To investigate BSkG1 shell effects, we consider the usual neutron and proton shell gaps $\delta_{2n/p}(N, Z)$, defined as

$$\delta_{2n}(N_0, Z) = S_{2n}(N_0, Z) - S_{2n}(N_0 + 2, Z), \quad (17a)$$

$$\delta_{2p}(N, Z_0) = S_{2p}(N, Z_0) - S_{2p}(N, Z_0 + 2), \quad (17b)$$

where $S_{2n/p}$ are the two-neutron/-proton separation energies. We recall that the $\delta_{2n/p}$ serve as an indicator for shell closures, but that they are not measures of the size of the gap in the single-particle spectrum as they are sensitive to any structural change between the three nuclei whose masses enter Eq. (17) [93,94]. In particular, there is the phenomenon of “mutually enhanced stability” that is observed as a peak of the experimental $\delta_{2n/p}$ values for doubly-magic nuclei [95,96]. In mean-field models, it can be partially explained by the onset of deformation in adjacent nuclei [93], but its description is significantly improved when including rotational and vibrational corrections of some form [94,97,98], as the latter also tend to grow when going away from a doubly-magic nucleus. This phenomenon is superposed on the effect of possible quenching of the concerned shell closure that would also lead to a reduction of the $\delta_{2n/p}$ values when going to weakly-bound nuclei [94].

Figure 4 compares the $\delta_{2n/p}$ values across spherical shell closures for the BSkG1, HFB-21 and HFB-27 sets for the chains of heavy semi-magic nuclei, as well as available experimental data. All three mass models produce similar values for the $N_0 = 50, 82$ and $Z_0 = 50, 82$ gaps, agreeing with experimental values about equally well.

The situation is different for the $N_0 = 126$ and $N_0 = 184$ shell gaps. For the latter, no experimental information is available and the three models produce

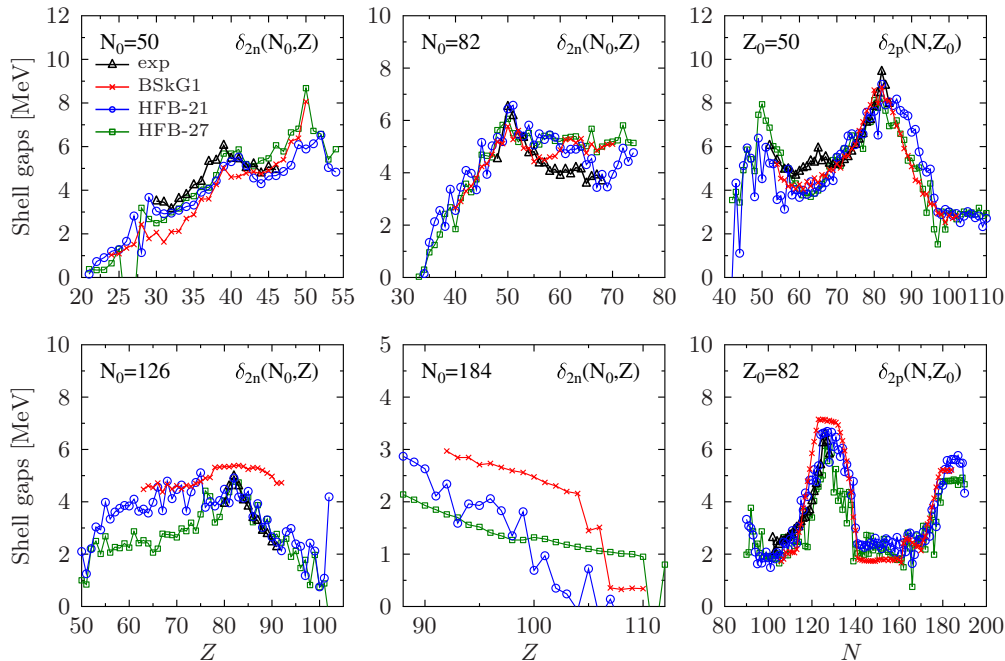


Fig. 4 (Color online) Shell gaps (see text) as obtained with the BSkG1 (red crosses), HFB-21 (blue circles) and HFB-27 (green squares) mass models. Available experimental data [17] are indicated by black triangles.

strikingly different predictions. For the $N_0 = 126$ gap, both HFB-21 and HFB-27 reproduce the known experimental data rather well, but produce different predictions for proton-deficient nuclei. Across the whole range of proton numbers, however, the BSkG1 model exhibits a structure that is qualitatively different from the HFB-21 and HFB-27 models.

4.2.3 Deformation

Global properties We start by discussing nuclear deformation in the BSkG1 model in a global fashion. The top left panel of Fig. 5 shows the quadrupole deformation β of Eq. (14a) for all calculated nuclei. Note that this quantity only indicates the size of the quadrupole deformation, and cannot discern between prolate, oblate or triaxial shapes. To determine the impact of axial-symmetry breaking on the final outcome, we have also performed calculations restricting the nuclei to axial quadrupole moments⁵. The energy differences between these and our unrestricted calculations are shown in the top right panel of Fig. 5. We see that a large number of nuclei are found to gain from a triaxial deformation at least 500 keV in binding energy. This implies that the parameterization makes significant use of non-axial

degrees of freedom to reproduce the known masses: restricting the nuclear shape to axial deformations worsens the rms mass deviation by more than 100 keV.

Looking more in detail, we observe several regions where a triaxial deformation manifests itself. The largest energy gain, up to 2.5 MeV, is observed for the neutron-rich $Z \sim 43$ isotopes. We also find rather deep triaxial minima in the neutron deficient $A \sim 70$ region with energy gains on the order of 1.5 MeV. Further “ribbons” of triaxiality can be seen just below the $N = 82$ and $N = 126$ shell closures, as well as below the $Z = 82$ magic number. Two intriguing regions are the islands around $Z \sim 96 - 100$ for extremely neutron-deficient and neutron-rich nuclei. Finally, we see that several very light nuclei with $Z \leq 20$ also acquire triaxial deformation, often due to the rotational correction, as discussed below.

To the best of our knowledge, no similar global survey of triaxial deformation exists for models based on Skyrme EDFs. We find that regions of triaxial deformation are generally centered in the same location as found in both microscopic-macroscopic calculations [73, 99], Gogny-HFB calculations based on the D1M mass model [12,100] and covariant density functional theory [101]. The energy gains due to triaxial deformation that we find are generally comparable to Gogny results, but significantly larger than those encountered in microscopic-macroscopic calculations where energy

⁵Multipole moments of higher order were left unconstrained, such that the configurations were not necessarily entirely axially symmetric.

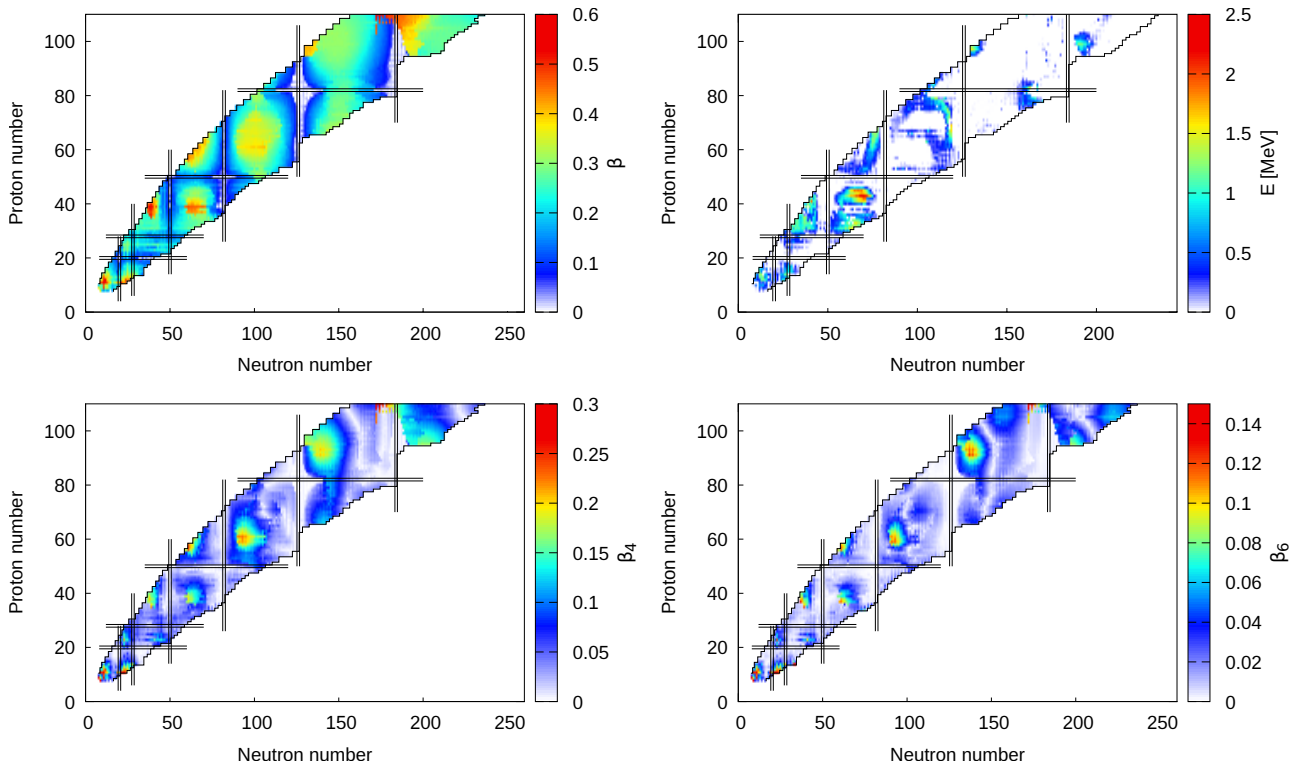


Fig. 5 (Color online) Top-left panel: Quadrupole deformation β . Top-right panel: Binding energy differences between unrestricted calculations and calculations restricted to axial quadrupole deformations. Bottom-left panel: hexadecapole deformation β_4 . Bottom-right: hexacontatetrapole deformation β_6 . All quantities extracted from BSkG1 calculations.

gains are typically smaller than 350 keV and consequently an overall smaller number of triaxial minima is found [73]. More localized studies are more numerous than the (rare) global surveys of triaxiality. Such studies generally concentrate on regions where the BSkG1 model also predicts triaxial ground state deformation, such as the Ge and Se isotopes in the $A \sim 70$ region [102–105], the Kr, Sr, Zr, Mo and Ru isotopes in the $A \sim 100$ region [106–111], and the neutron-rich rare-earths around $A \sim 190$ [112–114].

We will compare our nuclear ground state deformations to experimental data below, but we mention here already that triaxial deformation is known to also play a role at finite excitation energy: the prime example being collective γ -bands [115] that have been documented across the nuclear chart. More exotic examples include chiral bands [116], various kinds of “wobbling” bands [117–119] as well as bands based on superdeformed triaxial configurations [120,121]. The calculation of such configurations is out of the scope of this paper, but we observe that these phenomena have typically been found in regions of the nuclear chart where the BSkG1 model indicates the importance of triaxial deformation.

Although the nuclear quadrupole moments represent the dominant deformation mode, any higher order multipole moments that are unrestricted by symmetry generally take non-zero values as well. For heavy nuclei, we find significant non-zero values for β_ℓ up to at least $\ell = 10$, although the deformations naturally become smaller with increasing ℓ . For example, we show in the bottom panels of Fig. 5 the sizes of the hexadecapole ($\ell = 4$) and hexacontatetrapole deformations ($\ell = 6$) across the nuclear chart: there are several regions where the self-consistent optimization utilized these shape degrees of freedom to lower the energy of the nucleus. We do not show results for moments beyond $\ell = 6$: the associated spherical harmonics oscillate very rapidly and numerically calculated integrals involving them are not very precise on a coarsely discretized cubic coordinate-space mesh as used here.

Comparison to experiment Most of the experimental information on nuclear deformation concerns the quadrupole moments. Figure 6 compares the calculated quadrupole moment β for 319 even-even nuclei with the tabulated deformation parameters of Ref. [122], extracted from measured $B(E2)$ transition rates. The quadrupole deformation β lies roughly between 0.1 and 0.4 for the

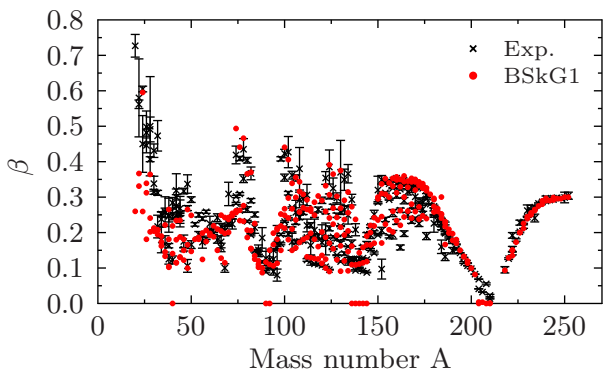


Fig. 6 (Color online) Experimental deformations (black crosses) of the 319 even-even nuclei of Ref. [122], deduced from the $B(E2)$ transitions to the first excited 2^+ state. Total quadrupole deformation (red crosses) as calculated with BSkG1.

majority of experimental data points. The BSkG1 model provides a satisfactory description of such well-deformed nuclei, and works particularly well for the heavier nuclides beyond $A \sim 160$. For experimental data points with either small ($\beta \leq 0.1$) or for light nuclei with large deformation ($\beta \geq 0.4$), the model performs significantly worse. This is especially visible for the light nuclei below $A \sim 50$ and around $A \sim 208$ near the $N = 126$ shell closure. This deficiency is not unexpected, as such nuclei typically cannot be modelled as rotors with static (quadrupole) deformation. In fact, for nuclei with $\beta \leq 0.1$, the excitation spectrum usually indicates that the first 2^+ state is either vibrational or a multi-quasiparticle excitation, such that the $B(E2, 2^+_1 \rightarrow 0^+_1)$ cannot be used to attribute a deformation to the ground state. A more appropriate description of such nuclei would require an improved treatment of collective degrees of freedom, beyond what our description in terms of a single mean-field state (with phenomenological corrections) can provide.

Direct experimental information on triaxial deformation of the nuclear ground state is elusive, but exists for a limited set of nuclei. Through careful analysis of a large number of $E2$ transitions observed in Coulomb excitation experiments, quadrupole rotational invariants of the nuclear ground state can be deduced. These invariants can be linked to the deformation of the nucleus in the intrinsic frame [142,143], allowing for the extraction of the mean triaxiality angle γ . We compare such experimental values of 26 (even-even) nuclei for γ [141] to the values obtained from calculations with BSkG1 in the bottom panel of Fig. 7. To provide additional context, we also compare the calculated size of the quadrupole deformation β to values from Nudat calculated from evaluated $B(E2; 2^+_1 \rightarrow 0^+_1)$

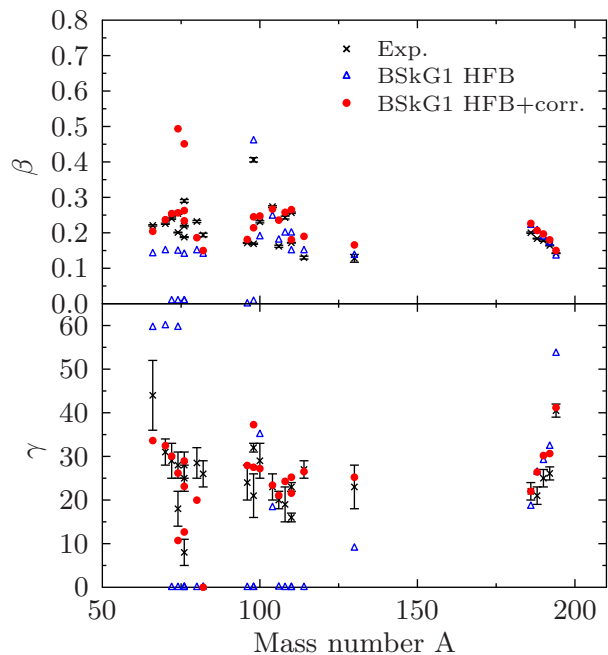


Fig. 7 (Color online) Calculated quadrupole deformation, with (red circles) and without (blue triangles) the rotational correction, compared to experimental information (black crosses). Top panel: quadrupole deformation β with experimental information from Nudat [123] for ^{66}Zn [124], ^{70}Ge [125], ^{72}Ge [126], ^{74}Ge [127], ^{76}Ge [128], $^{74,76}\text{Kr}$ [129], $^{76,80,82}\text{Se}$ [130], ^{98}Sr [131], ^{96}Mo [132], ^{98}Mo [133], ^{100}Mo [134], ^{104}Ru [135], ^{110}Cd [136], ^{114}Cd [137], $^{106,108,110}\text{Pd}$ [138], ^{130}Xe [139], $^{186,188,190,192}\text{Os}$ and ^{194}Pt [140]. Bottom panel: triaxiality angle γ , with experimental data points extracted from measured sets of transitional and diagonal $E2$ matrix elements [141] (see text) for the same nuclei.

transition probabilities [123]. The global agreement between experiment and the full BSkG1 model (including the rotational correction) is excellent for both β and γ . We note in particular the reproduction of the trend of increasing γ and decreasing β with mass number in $^{186,188,190,192}\text{Os}$ and ^{194}Pt [140].

Impact of the rotational correction The results discussed in the previous paragraphs are influenced significantly by the contribution of the rotational correction. This phenomenological correction favors (i) larger values of β and (ii) triaxial shapes over axial ones. Pure mean-field calculations (*i.e.* without E_{corr} in Eq. 1), would result in a larger number of spherical nuclei, smaller overall quadrupole deformations and a smaller number of triaxial deformations. This is perhaps most noticeable by the appearance of small deformations for light semi-magic nuclei in the top left panel of Fig. 5; in particular, we find no spherical minima for nuclei with $N = 28$ and/or $Z = 28$. This finding, however, does not mean

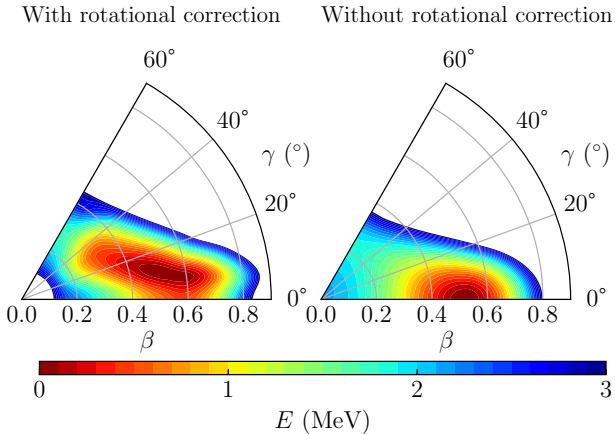


Fig. 8 Left panel: deformation energy of ^{24}Mg relative to its ground state as obtained with BSkG1. Right panel: energy surface with the rotational correction removed, $E_{\text{tot}} - E_{\text{rot}}$. Both panels are normalized to their respective minimum.

that these nuclei are predicted to be static rotors, but rather signals that these nuclei are so soft that correlation energies are important for their accurate modelling [97]. Another striking effect of the rotational correction is the appearance of large deformation for light nuclei, such as a minimum at $\beta = 0.590$ for ^{24}Mg .

Since the rotational correction intends to mimic the impact of symmetry restoration, these features of our model emerge naturally, even though they might be surprising at a first glance. Rotational symmetry-restoration through projection techniques [66] generally result in lower energies for less symmetric configurations, producing slightly deformed minima for nuclei with spherical mean-field minima and often very deformed minima for light nuclei [97]. We illustrate the effect of the rotational correction in Fig. 8, where we show the energy of ^{24}Mg in the β - γ plane. Without this correction, the configuration with minimum mean-field energy is axially symmetric prolate with $\beta \sim 0.5$. If the correction is included however, the overall minimum is triaxial with $\beta \sim 0.59$, which is comparable to the measured transition charge quadrupole moment $\beta = 0.613(14)$ [123]. We see that our example in Fig. 8 is qualitatively similar to the full angular-momentum projected calculations based on the triaxial mean-field states of Refs. [144] and [145] that are based on EDFs of Skyrme and Gogny-type, respectively⁶.

Finally, we note that the agreement between COULEX data and the BSkG1 model in Fig. 7 is at least partially due to the inclusion of the rotational correction. Without it, several of these nuclei would exhibit pro-

⁶While we cite only EDF-based examples, the same effect is present for projected mean-field calculations in shell-model valence spaces [146].

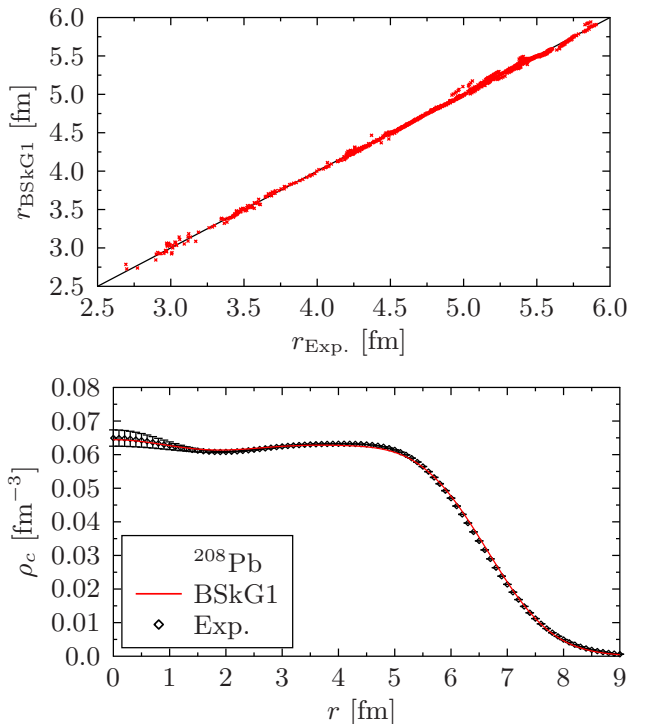


Fig. 9 (Color online) Top panel: comparison of BSkG1 charge radii to experimental values taken from Ref. [86]. Lower panel: calculated radial charge density of ^{208}Pb compared to experimental data of Ref. [147].

late ($\gamma = 0^\circ$) or oblate ($\gamma = 60^\circ$) minima, generally at a lower value of β than experimental data indicates. We take this as an indication that the modelling of these nuclei in terms of a pure mean-field state is insufficient and beyond-mean-field effects are important, even if they are only schematically included as we do here.

4.2.4 Charge distribution

Charge radii are obtained with an accuracy similar to those of the BSk mass models, *i.e.* with an rms deviation of 0.024 fm with respect to the 884 measured values [86]. We show the agreement between known and calculated charge radii in the top panel of Fig. 9. We recall that the charge densities are obtained through folding of the neutron and proton point densities with appropriate form factors (Sec. 2.1.3).

As a further point of comparison, we show in the bottom panel of Fig. 9 the calculated charge distribution of ^{208}Pb , to be compared to the measured values of Ref. [147]. The overall agreement is excellent, a quality shared with the BSk models [52]. It should also be emphasized that we obtain a neutron skin thickness for ^{208}Pb of 0.18 fm, as expected from the symmetry energy constrained to $J = 32$ MeV [52].

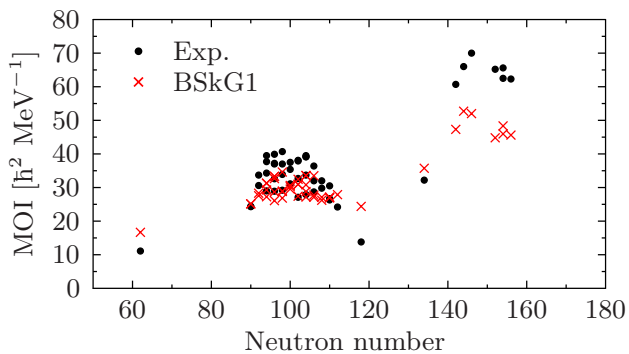


Fig. 10 Belyaev MOI obtained with BSkG1 (red crosses) compared to the experimental data (black dots) compiled in Refs. [78–80].

4.2.5 Moments of inertia and pairing properties

Figure 10 compares the calculated MOI to the 48 experimental values included in the objective function, as discussed in Sec. 4.1. The calculated MOIs systematically underestimate the experimental data by about 10%, particularly for the heavy $N \sim 150$ isotopes, but provide an overall acceptable description of the rotational properties of these even-even nuclei⁷. In addition, we remark that it is natural that our calculations somewhat underestimate the experimental values; if we would consider the Thouless-Valatin MOI instead of the simple Belyaev MOI, the calculated values would increase by roughly 30% [171].

To estimate the BSkG1 pairing effects, we compare the calculated five-point mass differences in Fig. 11 with experimental values for a representative sample of nuclei, namely the isotopic chains of Ca, Zr, Nd, Hg, and Fm. The overall size of the mass differences, for both protons and neutrons, is reasonably well described.

The overall agreement with experiment of the MOI and the mass differences in Figs. 10 and 11 is a direct consequence of the inclusion of the former into the objective function (Eq. 16). Without such a constraint, the model readjustment to only the absolute nuclear masses would have resulted in an overall lower rms on the known masses, $\sigma(M) \sim 0.66$ MeV, but with unrealistically large odd-even staggering and unrealistically small MOIs. At the other extreme, readjusting the pairing properties only on the odd-even staggering of the masses would result in severe underbinding for the majority of open-shell nuclei with small or vanishing deformations, mostly due to the absence of correlations beyond the rotational correction [77]. An increase of the pairing strength would then help the fit to emulate

⁷The comparison of the MOI of triaxial configurations with experiment is not trivial, see Appendix B.

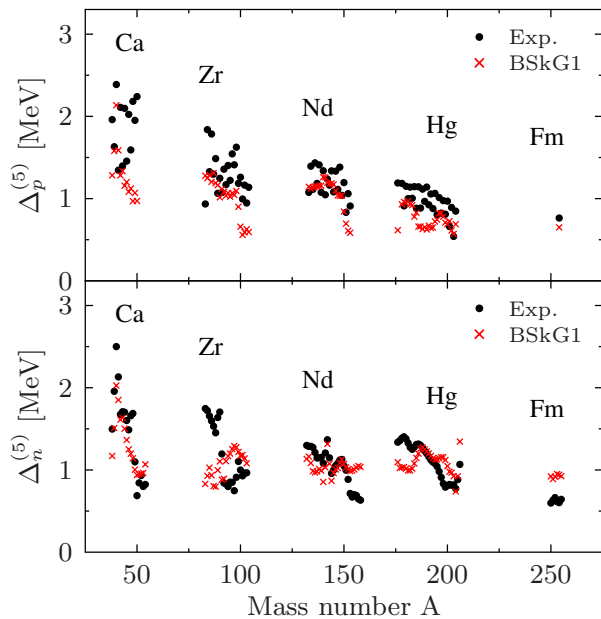


Fig. 11 (Color online) Comparison between the five-point proton (top) and neutron (bottom) mass differences $\Delta_{n,p}^{(5)}$ for isotopes of Ca, Zr, Nd, Hg, and Fm, as obtained from experiment (black dots) and BSkG1 (red crosses).

the missing collective binding energy for such nuclei in a global fashion, while deteriorating the description of the local, more fine-grained, odd-even staggering effect. This would have impacted negatively not only the description of other quantities sensitive to the pairing strength, such as the nuclear level densities, fission barriers and the MOIs discussed here, but also our confidence in extrapolation of the results to exotic nuclei.

4.3 Nuclear matter properties

The main properties of infinite charge-symmetric or pure-neutron matter are listed in Table 2. As discussed in Sec. 4.1, some of these properties have been constrained to a given value or a restricted range during the fitting procedure in order to reproduce experimentally extracted information or predictions from ab-initio calculations, as discussed in Ref. [11]. These properties concern in particular the symmetry coefficient $J = 32$ MeV, the compressibility $K_v = 237.8$ MeV through the $\gamma = 0.3$ parameter of the Skyrme EDF of Eq. (5)[148], and the isoscalar effective mass $M_s^*/M = 0.86$. The Fermi wave number k_F is known to drastically affect the nuclear radii and for this reason has been adjusted to minimize the overall mean deviation between experimental and predicted charge radii. The other properties of infinite nuclear matter directly result from the adjustment procedure and are found to be

in relatively good agreement with values extracted from measurements or ab-initio calculations, as discussed below.

In Fig. 12 we show the equation of state for pure neutron matter calculated with BSkG1. Despite the (imposed) value of the symmetry coefficient J , the equation of state of neutron matter remains rather soft at high densities with respect to the ab-initio calculations of APR [149] and LS2 [150], but is in agreement with FP [151] and WFF [152]. Compared to the BSk21 and BSk27 interactions, BSkG1 is somewhat intermediate in stiffness, and comparable to the SLy4 interaction, also characterized with $J = 32$ MeV. The maximum mass of non-rotating NSs for the BSkG1 equation of state is estimated to reach $1.79 M_{\odot}$, assuming the NSs are in β -equilibrium at zero temperature. This value is certainly below the observed limit of $2.08 \pm 0.07 M_{\odot}$ for pulsar PSR J0740+66220 [153]. Higher values of the symmetry coefficient J are not favored either by mass fits [11], or by ab-initio calculations of infinite neutron matter at low density (see the tendency for BSkG1 to underestimate ab-initio calculations in the insert of Fig. 12). A compatible stiffer equation of state, and hence higher NS masses, can be obtained by including density-dependent t_4 and t_5 terms in the EDF, as found with the BSk interactions starting from BSk18 [154]. Also note that the symmetry coefficient $J = 32$ MeV and slope $L = 51.7$ MeV are found to be fully compatible with the experimental constraints from heavy-ion collisions [155], neutron-skin thickness in Sn isotopes [156] and the analysis of the giant dipole resonance [157, 158], as summarized in Refs. [11, 157, 159].

As shown in Table 2, the fit led to an isoscalar effective mass at the saturation density of $M_s^*/M = 0.86$ in good agreement with the values obtained by the EBHF calculations of Ref. [82, 83]. The isovector effective mass, M_v^*/M , that emerged from the fit is found to be lower than the isoscalar effective mass, which implies that the neutron effective mass is larger than the proton effective mass in neutron-rich matter. This mass hierarchy between neutrons and protons is consistent with measurements of the isovector giant dipole resonance [160], and has been confirmed in ab-initio many-body calculations [82, 161]. In particular, for BSkG1, the magnitude of the splitting $M_s^* - M_v^* = 0.091$ is in good agreement with such ab-initio estimates of 0.098. A similar splitting was found with BSk21 (0.09) and BSk27 (0.08), in contrast to SLy4 which is characterized by a negative splitting of -0.11 , *i.e.* an opposite mass hierarchy $M_p^* > M_n^*$. These splittings are also illustrated in Fig. 13 which compares, as a function of the density n , neutron and proton effective masses in symmetric nuclear matter ($\eta = (n_n - n_p)/(n_n + n_p) = 0$)

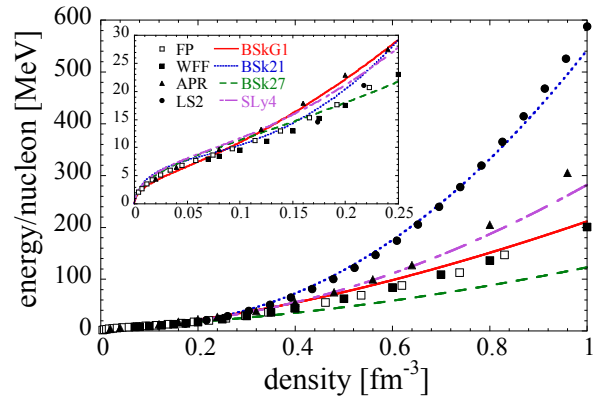


Fig. 12 (Color online) Zero-temperature equations of state for pure neutron matter with BSkG1, compared to ab-initio calculations referred to as FP, WFF, APR and LS2, as well as the BSk21 [88], BSk27 [15] and SLy4 [43] Skyrme parameterizations. FP corresponds to the ab-initio calculation of Friedman & Pandharipande [151], WFF to “UV14 plus TNI” of Ref. [152], APR of “A18 + δv + UIX*” in Ref. [149] and LS2 to V18 in Ref. [150]. The upper left insert is a zoom in view of densities below 0.25 fm^{-3} .

as well as in asymmetric matter with $\eta = 0.2$ and 0.4 obtained with the BSkG1, BSk21, BSk27, SLy4 interactions and the EBHF calculation of Ref. [161]. Most of the BSk forces, like BSk21 and BSk27, have an isoscalar effective mass at the saturation density constrained to 0.80, except BSk30-32 which adopted a higher value of 0.84. Note that the BSk21 non-linearity of $1/M_n^*$ and $1/M_p^*$ with density is due to the terms in t_4 and t_5 .

Fitting our forces to the mass data is not a sufficient condition for ensuring a realistic distribution of the potential energy per nucleon among the four two-body spin-isospin (S, T) channels in charge-symmetric infinite nuclear matter. Figure 14 shows this distribution for our new interaction as a function of the density and compares it with two different Brueckner-Hartree-Fock (BHF) calculations labeled “Catania 1” [150] and “Catania 2” [162]. For BSkG1, as well as BSk21, BSk27 and SLy4, the energies are calculated using the expression from Ref. [160], setting the coupling constants C_t^{sT} to zero for consistency with the choices made for the energy density of Eq. (5) [6, 85]. Given the evident uncertainty in what the real distribution actually is, the level of agreement we have found with our new BSkG1 interaction can be regarded as satisfactory, and significantly better than that obtained with the SLy4 functional, in particular for the $T = 1$ channels.

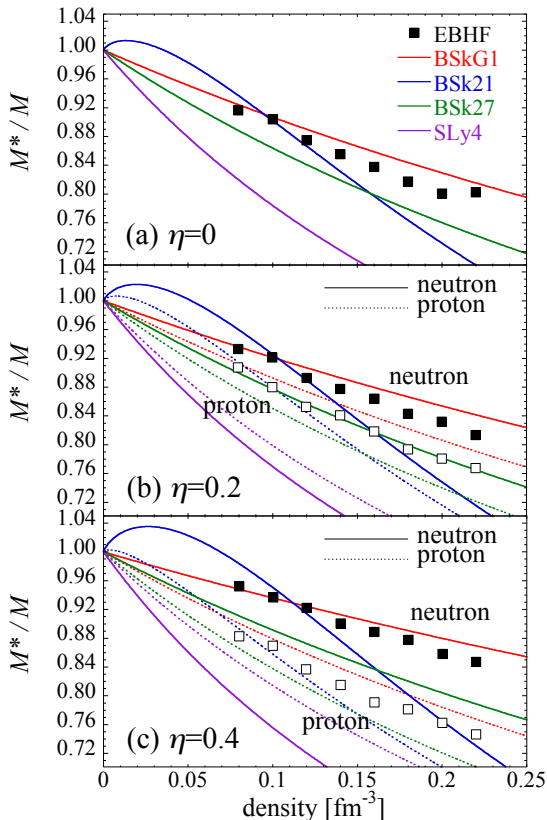


Fig. 13 (Color online) Neutron and proton effective masses in symmetric nuclear matter (a) as well as in asymmetric matter with an asymmetry $\eta = 0.2$ (b) and 0.4 (c) obtained with the BSkG1 (red lines), BSk21 (blue lines), BSk27 (green lines) and SLy4 (purple lines). For asymmetric matter, the neutron effective masses are shown with solid lines and the proton ones with dashed lines. The EBHF calculations of Ref. [161] are shown by squares for comparison (full and open squares correspond to the neutron and proton effective masses, respectively).

4.4 Application to the r-process nucleosynthesis

As an application of the new mass model, abundance distributions resulting from the r-process nucleosynthesis in NS mergers have been calculated with BSkG1 masses. The neutron capture and photoneutron astrophysical rates have been calculated for all nuclei with $8 \leq Z \leq 110$ lying between the proton and neutron drip lines on the basis of the ground state properties obtained with the BSkG1 mass model. Both the dynamical and disk ejecta of a NS binary system have been considered [89,90], as detailed below.

In the case of the dynamical ejecta, the same model as described in Ref. [91] and corresponding to a symmetric $1.365\text{--}1.365M_{\odot}$ binary system obtained with the SFHo equation of state [163] is adopted. Like in Ref. [91],

we consider two distinct scenarios reflecting the possible impact (or not) of neutrino absorption on the initial neutron-richness of the dynamical ejecta. In scenario I, all weak interactions on free nucleons are neglected and the mean initial electron fraction at the time the temperature has dropped below 10 GK corresponds to $\langle Y_e \rangle = 0.03$. This case is expected to mimic the nucleosynthesis from NS-black hole (BH) mergers or the prompt collapse of mass-asymmetric NS-NS mergers. In the second case (scenario II), weak nucleonic interactions are incorporated following the parametric approach of Ref. [164], in terms of prescribed neutrino luminosities and mean energies, but guided by the hydrodynamical simulations of Ref. [165] which includes a self-consistent approximated treatment of neutrino emission and absorption. This scenario is characterized with $\langle Y_e \rangle = 0.23$ and consequently gives rise to an r-process nucleosynthesis less efficient than in scenario I. Details about the nucleosynthesis calculations, additional nuclear inputs and the astrophysical scenario can be found in Ref. [91]. For both scenarios, the abundance distribution of the ejected material obtained with BSkG1 reaction rates is shown in Fig. 15 and compared to those found with the HFB-21 nuclear inputs [88], as used in Ref. [91]. Note that in both simulations the same β -decay rates as well as β -delayed neutron emission probabilities are taken from the relativistic mean-field model of Ref. [166]. Both mass models are found to give rise to abundance distributions that reproduce well the r-process peaks and the rare-earth bump. The BSkG1 masses tend to produce more nuclei around $A \simeq 140$, as well as Pb-group elements and actinides, essentially due to its stronger shell effect around $N = 184$ (as discussed in Sec. 4.2.2) which causes a larger accumulation of nuclei along the super-heavy $N = 184$ bottleneck during the neutron irradiation.

In addition to the dynamical ejecta, the neutrino and viscously driven outflows generated during the post-merger remnant evolution of the relic BH-torus system can be expected to give rise to a significant ejection of $A \geq 80$ r-process-rich material [90]. Full details about the hydrodynamical simulations can be found in Ref. [90]. We consider here a representative sample of 2075 trajectories ejected from a system characterized by a torus mass of $M_{\text{torus}} = 0.1M_{\odot}$ and a $3M_{\odot}$ BH (corresponding to the M3A8m1a5 model of Ref. [90]). The total mass ejected from the BH-torus system amounts to $2.5 \times 10^{-2} M_{\odot}$ and the outflow is characterized by a mean initial electron fraction $\langle Y_e \rangle = 0.24$.

The impact of the new masses on the composition of the BH-torus disk ejecta is shown in Fig. 15c where both mass models are seen to give rise to rather similar abundance distributions, especially around the second

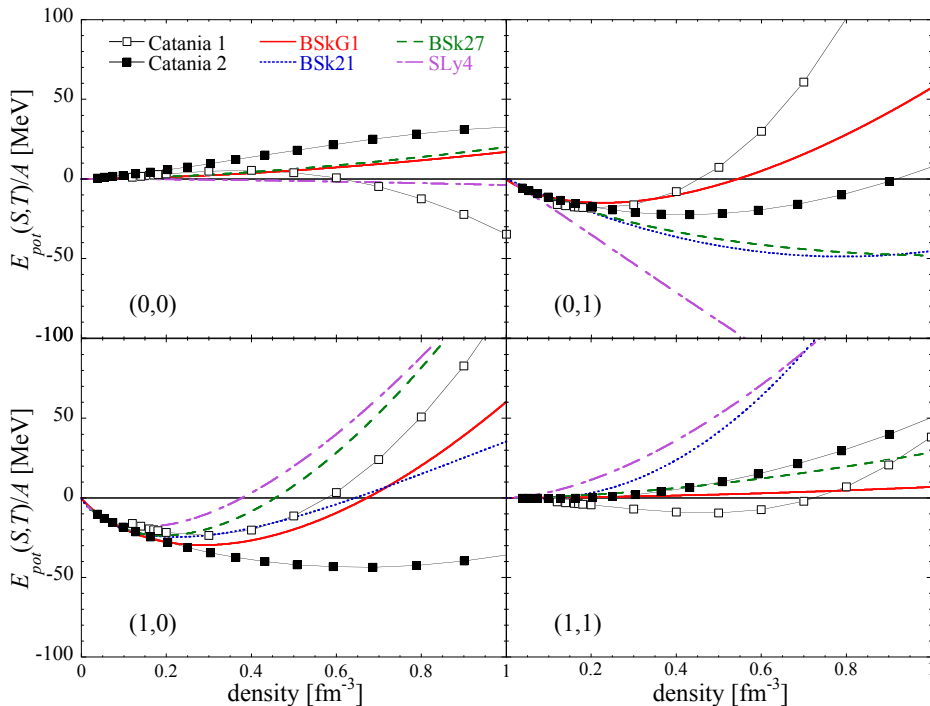


Fig. 14 (Color online) Potential energy per particle E_{pot}/A in each (S,T) channel as indicated as a function of density for charge-symmetric infinite nuclear matter for BSkG1, BSk21 [88], BSk27 [15] and SLy4 [43]. The open and solid squares correspond to the “Catania 1” [150] and “Catania 2” BHF calculations [162], respectively.

and third r-process peaks. BSkG1 masses tend to produce slightly less rare-earth elements than HFB-21.

5 Conclusions and outlook

5.1 Conclusions

We have presented the BSkG1 mass model, based on an energy density functional of the Skyrme type. The BSkG1 interaction has been adjusted on essentially all known nuclear masses, rendering the model well-suited for nuclear applications. The model achieves an rms deviation of 0.741 MeV on the 2457 known masses of the AME2020 database [17] and an rms deviation of 0.0239 fm on the 884 charge radii from Ref. [86]. To obtain realistic pairing strengths, we have included experimental information on the moment of inertia of a set of heavy nuclei in the adjustment procedure, resulting in a fair description of the pairing and rotational properties across the nuclear chart. We have in addition shown that the model reproduces well the available experimental data on all quadrupole degrees of freedom, i.e. data on β and γ .

Finally, the model offers a reasonable description of nuclear matter properties, as predicted by modern ab-

initio calculations, though with a relatively soft equation of state for infinite neutron matter.

These qualities render the new model competitive with those based on the older BSk effective interactions. While several of the latter (notably HFB-27 based on the BSk27 interaction) achieve somewhat lower overall rms deviations on the nuclear masses, the new model presents a significant step forward in multiple ways. First, we include for the first time triaxial deformation throughout the model adjustment. Second, the coordinate-space representation results in an excellent numerical precision as compared to an expansion in a limited set of harmonic oscillator states and results in much smoother trends for the separation energies. Third, the model can be used for applications that rely on a coordinate-space representation without ambiguity.

To readjust the parameters of the model, we needed to perform repeated three-dimensional calculations in a large single-particle basis. To offset the inherent computational cost, we presented a new adjustment procedure guided by a committee of multilayer neural networks. Each neural network provides us with a computationally cheap estimate of observables as a function of the parameters, and directs us easily towards its preferred candidate set. We improve the training of these networks through active learning on a growing set of self-

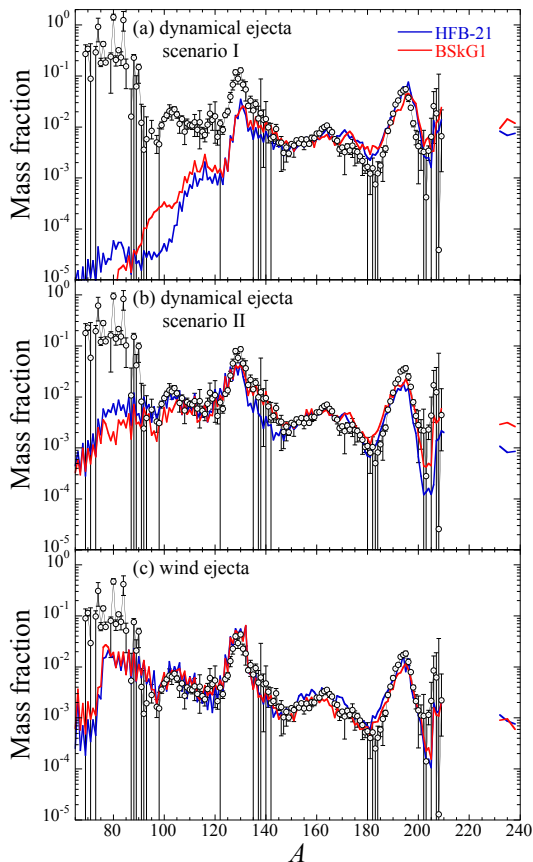


Fig. 15 (Color online) (a) Mass fraction of the $4.9 \times 10^{-3} M_{\odot}$ of material ejected in scenario I of the $1.365\text{--}1.365 M_{\odot}$ NS-NS merger model as a function of the atomic mass A . The red curve obtained with the BSkG1 nuclear masses and corresponding neutron capture and photoneutron rates is compared to the results obtained with HFB-21 [88] (blue curve). The solar system r -abundance distribution with corresponding error bars (open circles), arbitrarily normalized to the HFB-21 predictions in the $A \simeq 164$ region, is shown for comparison [167]. (b) Same as (a) for scenario II of the dynamical ejecta. (c) Composition of the $2.5 \times 10^{-2} M_{\odot}$ of material ejected from the post-merger BH-torus remnant characterized by a torus mass of $0.1 M_{\odot}$ and a $3 M_{\odot}$ BH [90].

consistent calculations and by pooling the predictions of a few hundred committee members, the model adjustment is guided to the relevant region of the parameter space. The neural network is only used for the parameter adjustment. Once this procedure is complete, all presented results are derived from a self-consistent EDF calculation.

A particular strength of this approach is its reusability for different objective functions. The committee is able to propose a candidate parameter set for an arbitrary function of observables, provided the committee is sufficiently well-trained to reliably estimate them. We

exploited this feature to efficiently search for a compromise between the description of nuclear masses and realistic pairing strengths.

5.2 Outlook

This work opens multiple pathways to even more refined global mass models. The first such direction is the lifting of the remaining symmetry restrictions: the inclusion of reflection asymmetric and time-reversal breaking nuclear configurations. While the former are expected to play a role for ground states in limited regions of the nuclear chart, the latter are relevant for the description of all nuclei with an odd neutron and/or odd proton number. Even though these constitute the majority of all nuclei, the effects of time-reversal breaking have never been studied in a global fashion. These will mainly add a correction to the odd-even staggering of masses that for BSkG1 is governed by pairing correlations. Current efforts in this direction are ongoing.

We have limited ourselves here to a global discussion of quadrupole deformation, charge radii and nuclear masses. A second path concerns the investigation with the BSkG1 model of other quantities that are known to impact astrophysical applications, and in particular the description of fission. We have shown the impact of triaxiality on the nuclear ground state, but this degree of freedom has long been known to affect the height of the first barrier for actinide nuclei [168]. Studies of relativistic functionals have shown that it can affect the second barrier systematically [169]. We suspect this is the case for Skyrme EDFs as well, as hinted in Ref. [170], but a global study is still missing. A dedicated study is necessary, whose conclusions can be fed back into the adjustment of future refinements of the mass model.

A third possible improvement concerns our treatment of collectivity. We do not account in any way for shape fluctuations and our approach to rotational collective motion remains highly approximate. Incorporating some degree of configuration mixing into the model, while very demanding, would allow for improvements on both types of collectivity. A more approachable strategy for nuclear vibration consists of incorporating a simple phenomenological prescription along the lines of Ref. [49]. The rotational correction could be improved by basing it on the Thouless-Valatin moments of inertia, which are known to capture the nuclear response to rotation more accurately than the Belyaev prescription [171]. The calculation of the former necessitates the breaking of time-reversal symmetry that has not been considered here. The extension to the full and systematic calculation of quadrupole and octupole correlation energies through the generate coor-

dinate method represents a difficult path that will have to be taken at some point.

Future improvements of the mass predictions will also require a better description of nuclei close to the $N = 126$ magic number, which are of special relevance to the r-process nucleosynthesis. A possible improvement could be found by following the same path as the BSk series, *i.e.* by including the density-dependent terms t_4 and t_5 in the energy density functional. The inclusion of these terms enables the creation of a functional with a low symmetry coefficient $J = 30$ MeV that also reproduces a stiff equation of state in infinite neutron matter [52]. Guided by ab-initio calculations of the pairing effects in infinite nuclear matter [82], more realistic forms of the pairing interactions [85] can also help improve the global coherence of the model.

All proposed additional ingredients could potentially influence the parameter adjustment with possibly interfering effects and might all require additional data to be added as constraints to the objective function. In order to maintain control of the parameter adjustment, they should not be added simultaneously. For this reason and their inherent computational complexity, implementing the ensemble of proposed improvements promises a long road ahead, along which the guidance of neural networks in the parameter fit will be essential.

Acknowledgements We are grateful to Magda Zielinska for extracting the experimental γ values from the literature and providing them to us for the preparation of Fig. 7, as well as for constructive comments on the manuscript. This work was supported by the Fonds de la Recherche Scientifique (F.R.S.-FNRS) and the Fonds Wetenschappelijk Onderzoek - Vlaanderen (FWO) under the EOS Project nr O022818F. The present research benefited from computational resources made available on the Tier-1 supercomputer of the Fédération Wallonie-Bruxelles, infrastructure funded by the Walloon Region under the grant agreement nr 1117545. S.G. and W.R. acknowledge financial support from the FNRS (Belgium). W.R. also acknowledges support by the U.S. DOE grant No. DE-SC0019521. Work by M.B. has been supported by the French Agence Nationale de la Recherche under grant No. 19-CE31-0015-01 (NEWFUN).

Appendix A: Coupling constants of E_{Sk}

The Skyrme energy density \mathcal{E} of Eq. (5) is determined by ten coupling constants, which are determined by the model parameters t_{0-3} , x_{0-3} , W_0 and W'_0 as follows:

$$C_0^{\rho\rho} = \frac{3}{8}t_0, \quad (\text{A.1a})$$

$$C_1^{\rho\rho} = -\frac{1}{4}t_0 \left(\frac{1}{2} + x_0\right), \quad (\text{A.1b})$$

$$C_0^{\rho\rho\rho\gamma} = \frac{3}{48}t_3, \quad (\text{A.1c})$$

$$C_1^{\rho\rho\rho\gamma} = -\frac{1}{24}t_3 \left(\frac{1}{2} + x_3\right), \quad (\text{A.1d})$$

$$C_0^{\rho\tau} = \frac{3}{16}t_1 + \frac{1}{4}t_2 \left(\frac{5}{4} + x_2\right), \quad (\text{A.1e})$$

$$C_1^{\rho\tau} = -\frac{1}{8}t_1 \left(\frac{1}{2} + x_1\right) - t_2 \left(\frac{1}{2} + x_2\right), \quad (\text{A.1f})$$

$$C_0^{\rho\Delta\rho} = -\frac{9}{64}t_1 + \frac{1}{16}t_2 \left(\frac{5}{4} + x_2\right), \quad (\text{A.1g})$$

$$C_1^{\rho\Delta\rho} = \frac{3}{32}t_1 \left(\frac{1}{2} + x_1\right) + \frac{1}{32}t_2 \left(\frac{1}{2} + x_2\right), \quad (\text{A.1h})$$

$$C_0^{\rho\nabla\cdot J} = -\frac{W_0}{2} - \frac{W'_0}{4}, \quad (\text{A.1i})$$

$$C_1^{\rho\nabla\cdot J} = -\frac{W'_0}{4}. \quad (\text{A.1j})$$

Appendix B: Further details on the rotational correction and the MOI

The rotational correction, Eq. (12a), depends on the calculation of $\langle \hat{J}_\mu^2 \rangle$ and \mathcal{I}_μ for all three principal axes of the nucleus. Formulas are available in the literature for even-even nuclei (see, e.g. [53, 58]). However, naively utilizing these expressions in our calculations is problematic for two reasons.

The first is purely technical: the calculation of \mathcal{I}_μ involves a summation over all possible two-quasiparticle excitations in the model space, weighted by the inverse of the sum of their quasiparticle energies. Unlike any other quantity discussed here, this sum is not naturally cut by the single-particle occupation factors. As our numerical implementation can only represent a fraction of the entire quasiparticle spectrum, we have introduced an additional cutoff for the rotational correction. We replace the matrix elements of the single-particle angular momentum operator \hat{j} that figure into the calculation of *both* $\langle \hat{J}_\mu^2 \rangle$ and \mathcal{I}_μ as

$$\langle k | \hat{j}_\mu | l \rangle \rightarrow f_{q,k}^{\text{MOI}} f_{q,l}^{\text{MOI}} \langle k | \hat{j}_\mu | l \rangle, \quad (\text{B.2})$$

$$f_{q,k}^{\text{MOI}} = \left[1 + e^{(\epsilon_k - \lambda_q - E_{\text{cut}})/\mu_{\text{MOI}}} \right]^{-1/4}, \quad (\text{B.3})$$

where the cut-off energy E_{cut} is identical to the one used in the pairing channel (Eq. 7), but $\mu_{\text{MOI}} = 1$ MeV.

The second problem affects the calculation of both quantities for odd- A and odd-odd nuclei. For the ground states of even-even nuclei, the expectation value of \hat{J}_μ^2 and the Belyaev MOI are purely collective in nature, *i.e.* non-zero values are generated by many nucleons as a result of the nuclear deformation. This picture is modified significantly by the presence of blocked quasiparticles, whose individual contributions to both \hat{J}_μ^2 and \mathcal{I}_B are

generally sizeable and cannot be considered as collective. Furthermore, the Belyaev MOI is fundamentally a quantity obtained from second-order perturbation theory of an HFB minimum. While its calculation can be generalized to include the possibility of blocked quasiparticles along the lines of Ref. [172], the validity of such an approach can be questioned. As a purely practical recipe to sidestep these issues, we calculate both \hat{J}_μ^2 and \mathcal{I}_B for odd- A and odd-odd nuclei by omitting the contributions from all blocked quasiparticles, mirroring the approach of Ref. [173].

Finally, we comment on the comparison of calculated (Belyaev) MOI with experimental data, as we do in Fig. 10. For axial configurations, the Belyaev MOI along the symmetry axis vanishes, while the two remaining values are equal; comparison to experiment is then straightforward. For triaxial nuclear configurations, we obtain however three non-zero, distinct values for the MOI. In those cases, we have chosen systematically the largest among the three values as the one to be compared to experiment. We have made this rather ad-hoc choice motivated by a naive semi-classical model of rotation, where the largest MOI produces the lowest-lying rotational excitations. As the experimental data is extracted from the excitation energy of the first 2^+ state in rotational nuclei, this seems to be the most appropriate choice.

Appendix C: Explanation of the supplementary material

We provide as supplementary material the file `Mass_Table_BSkG1.dat`, which contains the calculated ground state properties of all nuclei with $8 \leq Z \leq 110$ lying between the proton and neutron drip lines. Its content is summarized and explained in Tab. 4. A few additional remarks are in order:

- **Column 11/12:** A unique definition of the pairing gap exists only for HFB calculations with schematic interactions. To extract some information on the overall importance of the pairing correlations for a given nucleus, we use the uv -weighed average pairing gaps $\langle \Delta \rangle_{n/p}$ of Ref. [174].
- **Column 16:** we report only the largest MOI among all three directions, *i.e.* the file contains $\max_{\mu=x,y,z} \{\mathcal{I}_\mu\}$.
- **Column 17/18:** as discussed in Sec. 2.2.3, we construct auxiliary states for odd- A and odd-odd nuclei through a self-consistent blocking procedure. To make these calculations reproducible, we provide for such nuclei the parity quantum number of the blocked quasiparticles.

References

1. M. Arnould, S. Goriely, *Prog. Part. Nuc. Phys.* **112**, 103766 (2020).
2. M. Arnould, S. Goriely, K. Takahashi, *Phys. Rep.* **450**, 97 (2007).
3. J. Erler *et al.*, *Nature* **486**, 509 (2012).
4. R. Wang and L.-W. Chen, *Phys. Rev. C* **92**, 031303(R) (2015).
5. L. Neufcourt, Y. Cao, S. A. Giuliani, W. Nazarewicz, E. Olsen, and O. B. Tarasov, *Phys. Rev. C* **101**, 044307 (2020).
6. M. Bender, P.-H. Heenen, and P.-G. Reinhard, *Rev. Mod. Phys.* **75**, 121 (2003).
7. P. Klüpfel, P.-G. Reinhard, T. J. Bürvenich, and J. A. Maruhn, *Phys. Rev. C* **79**, 034310 (2009).
8. M. Baldo, L. M. Robledo, P. Schuck, and X. Viñas, *Phys. Rev. C* **87**, 064305 (2013).
9. J. Erler, C. J. Horowitz, W. Nazarewicz, M. Rafalski, and P.-G. Reinhard, *Phys. Rev. C* **87**, 044320 (2013).
10. M. Kortelainen *et al.*, *Phys. Rev. C* **89**, 054314 (2014).
11. S. Goriely, N. Chamel, and J. M. Pearson, *Phys. Rev. C* **93**, 034337 (2016).
12. S. Goriely, S. Hilaire, M. Girod and S. Péru, *Phys. Rev. Lett.* **102**, 242501 (2009).
13. K. Bennaceur, J. Dobaczewski, T. Haverinen, and M. Kortelainen, *J. Phys. G: Nucl. Part. Phys.* **47**, 105101 (2020).
14. S. Goriely and R. Capote, *Phys. Rev. C* **89**, 054318 (2014).
15. S. Goriely, N. Chamel, and J. M. Pearson, *Phys. Rev. C* **88**, 061302(R) (2013).
16. M. Wang *et al.*, *Chin. Phys. C* **41**, 3 (2017).
17. M. Wang *et al.*, *Chin. Phys. C* **45**, 3 (2021).
18. E. Verstraelen *et al.*, *Phys. Rev. C* **100**, 044321 (2019).
19. S. Ówiok, P.-H. Heenen and W. Nazarewicz, *Nature* **433**, 705 (2005).
20. D. Baye and P.-H. Heenen, *J. Phys. A: Math. Gen.* **19**, 2041 (1986).
21. W. Ryssens, P.-H. Heenen and M. Bender, *Phys. Rev. C* **92**, 064318 (2015).
22. A. Arzhanov, T. R. Rodríguez and G. Martínez-Pinedo, *Phys. Rev. C* **94**, 054319 (2016).
23. C. Simenel and A. S. Umar, *Prog. Part. Nuc. Phys.* **103**, 19 (2018).
24. G. Scamps and C. Simenel, *Nature* **564**, 382 (2018).
25. P. Magierski and P.-H. Heenen, *Phys. Rev. C* **65**, 045804 (2002).
26. P. Gögelein and H. Müther, *Phys. Rev. C* **76**, 024312 (2007).
27. H. Pais, W. G. Newton, and J. R. Stone, *Phys. Rev. C* **90**, 065802 (2014).
28. B. Schuetrumpf, G. Martínez-Pinedo, Md. Afibuzzaman, and H. M. Aktulga, *Phys. Rev. C* **100**, 045806 (2019).
29. T. Bayram, S. Akkoyun and Ş. Şentürk, *Phys. of Atom. Nucl.* **81**, 288 (2018).
30. R.-D. Lasserri, D. Regnier, J.-P. Ebran, and A. Penon, *Phys. Rev. Lett.* **124**, 162502 (2020).
31. N. Schunck, J. D. McDonnell, D. Higdon, J. Sarich, and S. M. Wild, *Eur. Phys. J. A* **51**, 169 (2015).
32. N. Schunck, K. R. Quinlan, and J. Bernstein, *J. Phys. G* **47**, 10 (2020).
33. Z. M. Niu and H.Z. Liang, *Phys. Lett. B* **778**, 48 (2018).
34. Z. M. Niu, H. Z. Liang, B. H. Sun, W. H. Long, and Y. F. Niu, *Phys. Rev. C* **99**, 064307 (2019).

Column	Quantity	Units	Explanation
1	Z	–	Proton number
2	N	–	Neutron number
3	M_{exp}	MeV	Experimental atomic mass excess
4	M_{th}	MeV	BSkG1 atomic mass excess
5	ΔM	MeV	$M_{\text{exp}} - M_{\text{th}}$
6	E_{tot}	MeV	Total binding energy, Eq. (1).
7	β_{20}	–	Deformation, Eq. (13).
8	β_{22}	–	Deformation, Eq. (13).
9	β	–	Deformation, Eq. (14a)
10	E_{rot}	MeV	Rotational correction, Eq. (12a).
11	$\langle \Delta \rangle_n$	MeV	Average neutron gap
12	$\langle \Delta \rangle_p$	MeV	Average proton gap
13	r_{BSkG1}	fm	Calculated rms charge radius
14	r_{exp}	fm	Experimental rms charge radius
15	Δr	fm	$r_{\text{exp}} - r_{\text{BSkG1}}$
16	\mathcal{I}_{MOI}	$\hbar^2 \text{ MeV}^{-1}$	Calculated MOI.
17	par(p)	–	Parity of protons qp. excitation
18	par(n)	–	Parity of neutrons qp. excitation

Table 4 Contents of the Mass-Table.BSkG1.dat file.

35. R. Bollapragada et al., J. Phys. G: Nucl. Part. Phys. **48** 024001 (2021).
36. L. Neufcourt, Y. Cao, W. Nazarewicz, and F. Viens, Phys. Rev. C **98**, 034318 (2018).
37. L. Neufcourt, Y. Cao, W. Nazarewicz, E. Olsen, and F. Viens, Phys. Rev. Lett. **122**, 062502 (2019).
38. L. Neufcourt, Y. Cao, S. Giuliani, W. Nazarewicz, E. Olsen, and O. B. Tarasov, Phys. Rev. C **101**, 014319 (2020).
39. J. Bartel *et al.*, Nucl. Phys. A **386**, 79 (1982).
40. M. M. Sharma, G. Lalazissis, J. König, and P. Ring, Phys. Rev. Lett. **74**, 3744 (1995).
41. P.-G. Reinhard and H. Flocard, Nucl. Phys. A **584**, 467 (1995).
42. M. Kortelainen, T. Lesinski, J. More, W. Nazarewicz, J. Sarich, N. Schunck, M.V. Stoitsov, and S. M. Wild, Phys. Rev. C **82**, 024313 (2010).
43. E. Chabanat, P. Bonche, P. Haensel, J. Meyer, and R. Schaeffer, Nucl. Phys. A **635**, 231 (1998); Nucl. Phys. A **643**, 441(E) (1998).
44. M. Kortelainen, J. McDonnell, W. Nazarewicz, P.-G. Reinhard, J. Sarich, N. Schunck, M.V. Stoitsov, and S. M. Wild, Phys. Rev. C **85**, 024304 (2012).
45. S. J. Krieger, P. Bonche, H. Flocard, P. Quentin, and M. S. Weiss, Nucl. Phys. A **517**, 275 (1990).
46. B. A. Brown, W. A. Richter, and R. Lindsay, Phys. Lett. B **483**, 49 (2000).
47. S. Goriely and J. M. Pearson, Phys. Rev. C **77**, 031301(R) (2008).
48. S. T. Belyaev, Nucl. Phys. **24**, 322 (1961).
49. S. Goriely, M. Samyn, and J. M. Pearson, Phys. Rev. C **75**, 064312 (2007).
50. D. Peña-Arteaga, S. Goriely, and N. Chamel, Eur. Phys. J. A **52**, 320 (2016).
51. M. Bender, K. Rutz, P.-G. Reinhard, and J. Maruhn, Eur. Phys. J. A **7**, 467 (1999).
52. S. Goriely, N. Chamel, and J. M. Pearson, Phys. Rev. C **88**, 024308 (2013).
53. W. Ryssens, V. Helleman, M. Bender, and P.-H. Heenen, Comput. Phys. Commun. **187**, 175 (2015).
54. J. Dobaczewski, H. Flocard and J. Treiner, Nuc. Phys. A **422**, 103 (1984).
55. J. W. Negele, Phys. Rev. C **1**, 1260 (1970).
56. I. Sick, Phys. Lett. B **576**, 62 (2003).
57. H. Chandra, and G. Sauer, Phys. Rev. C **13**, 245 (1976).
58. P. Ring, P. Schuck, *The Nuclear Many-Body Problem*, (Springer Verlag, 1980).
59. W. Ryssens, Symmetry breaking in nuclear mean-field models, Ph.D. thesis, Université Libre de Bruxelles, 2016.
60. W. Ryssens, M. Bender, and P.-H. Heenen, MOCCa code (unpublished).
61. W. Ryssens, M. Bender, and P.-H. Heenen, Eur. Phys. J. A **55**, 93 (2019).
62. B. Gall, P. Bonche, J. Dobaczewski, H. Flocard, and P.-H. Heenen, Z. Phys. A **348**, 183 (1994).
63. P. Bonche, H. Flocard, and P.-H. Heenen, Comput. Phys. Commun. **171**, 49 (2005).
64. D. Baye, Phys. Rep. **565**, 1 (2015).
65. B. G. Carlsson, J. Dobaczewski, J. Toivanen and P. Veselý, Comp. Phys. Comm. **181**, 1641 (2010).
66. B. Bally and M. Bender, Phys. Rev. C **103**, 024315 (2021).
67. M. Bender *et al.*, J. Phys. G: Nucl. Part. Phys. **47**, 113002 (2020).
68. L. M. Robledo and G. F. Bertsch, Phys. Rev. C, **84**, 054302 (2011).
69. S. E. Agbemava, A. V. Afanasjev and P. Ring, Phys. Rev. C **93**, 044304 (2016).
70. Y. Cao, S. E. Agbemava, A. V. Afanasjev, W. Nazarewicz, and E. Olsen, Phys. Rev. C **102**, 024311 (2020).
71. N. Schunck, J. Dobaczewski, J. McDonnell, J. More, W. Nazarewicz, J. Sarich, and M. V. Stoitsov, Phys. Rev. C **81**, 024316 (2010).
72. K. J. Pototzky, J. Erler, P.-G. Reinhard, and V. O. Nesterenko, Eur. Phys. J. A **46**, 299 (2010).
73. P. Möller, R. Bengtsson, B. G. Carlsson, P. Olivius, and T. Ichikawa, Phys. Rev. Lett. **97**, 162502 (2006).
74. S. Perez-Martin and L. M. Robledo, Phys. Rev. C **78**, 014304 (2008).
75. F. Chollet, Deep Learning with Python (Manning Publications, Shelter Island, New York, 2017).

76. R. H. Byrd, R. B. Schnabel, and G. A. Shultz, *Math. Program.* **40**, 247 (1988).
77. S. Goriely, N. Samyn, and J. M. Pearson, *Nucl. Phys. A* **773**, 279 (2006).
78. J. Y. Zeng, T. H. Jin, and Z. J. Zhao, *Phys. Rev. C* **50**, 1388 (1994).
79. A. V. Afanasjev, J. König, P. Ring, L. M. Robledo, and J. L. Egido, *Phys. Rev. C* **62**, 054306 (2000).
80. J.M. Pearson, Y. Aboussir, A.K. Dutta, R.C. Nayak, M. Farine, F. Tondeur, *Nucl. Phys. A*, **528**, 1 (1991).
81. G. Colò, N.V. Giai, J. Meyer, K. Bennaceur, and P. Bonche, *Phys. Rev. C* **70**, 024307 (2004).
82. L. G. Cao, U. Lombardo, and P. Schuck, *Phys. Rev. C* **74**, 064301 (2006).
83. W. Zuo, A. Lejeune, U. Lombardo, and J.-F. Mathiot, *Nucl. Phys. A* **706**, 418 (2002).
84. J. Margueron, J. Navarro, and N. V. Giai, *Phys. Rev. C* **66**, 014303 (2002).
85. N. Chamel and S. Goriely, *Phys. Rev. C* **82**, 045804 (2010).
86. I. Angeli and K. P. Marinova, *At. Data Nucl. Data Tables* **99**, 69 (2013).
87. P. Möller and J.R. Nix, *At. Data Nucl. Data Tables* **39**, 213 (1988).
88. S. Goriely, N. Chamel, and J. M. Pearson, *Phys. Rev. C* **82**, 035804 (2010).
89. S. Goriely, A. Bauswein, and H.-T. Janka, *Astrophys. J. Lett.* **738**, L32 (2011).
90. O. Just, A. Bauswein, R. Ardevol-Pulpillo, S. Goriely, and H.-T. Janka, *Mon. Not. Roy. Astron. Soc.* **448**, 541 (2015).
91. J.-F. Lemaître, S. Goriely, A. Bauswein, and H.-T. Janka, *Phys. Rev. C* **103**, 025806 (2021).
92. R. Jodon, M. Bender, K. Bennaceur, and J. Meyer, *Phys. Rev. C* **94**, 024335 (2016).
93. M. Bender, T. Cornelius, G. A. Lalazissis, J. A. Maruhn, W. Nazarewicz, and P.-G. Reinhard, *Eur. Phys. J. A* **14**, 23 (2002).
94. M. Bender, G. F. Bertsch, and P.-H. Heenen, *Phys. Rev.* **78**, 054312 (2008).
95. N. Zeldes, T. S. Dumitrescu, and H. S. Köhler, *Nucl. Phys. A* **399**, 11 (1983).
96. V. Manea, J. Kartheim, D. Atanasov, M. Bender, K. Blaum, T. E. Cocolios, S. Eliseev, A. Herlert, J. D. Holt, W. J. Huang, Yu. A. Litvinov, D. Lunney, J. Menéndez, M. Mougeot, D. Neidherr, L. Schweikhard, A. Schwenk, J. Simonis, A. Welker, F. Wienholtz, and K. Zuber, *Phys. Rev. Lett.* **124**, 092502 (2020).
97. M. Bender, G. F. Bertsch and P.-H. Heenen, *Phys. Rev. C* **73**, 034322 (2006).
98. J.-P. Delaroche, M. Girod, J. Libert, H. Goutte, S. Hilaire, S. Péru, N. Pillet, and G. F. Bertsch, *Phys. Rev. C* **81**, 014303 (2010).
99. P. Möller, et al., *At. Data Nucl. Data Tables* **94**, 758 (2008).
100. S. Hilaire, private communication.
101. Y. L. Yang, Y. K. Wang, P. W. Zhao, Z. P. Li, arXiv:2108.13057 [nucl-th].
102. L. Guo, J. A. Maruhn and P.-G. Reinhard, *Phys. Rev. C* **76**, 034317 (2007).
103. S. F. Shen, S. J. Zheng, F. R. Xu and R. Wyss, *Phys. Rev. C* **84**, 044315 (2011).
104. T. Nikšić, P. Marević and D. Vretenar, *Phys. Rev. C* **89**, 044325 (2014).
105. G. H. Bhat, W. A. Dar, J. A. Sheikh and Y. Sun, *Phys. Rev. C*, **89**, 014328 (2014).
106. P. Bonche, H. Flocard, P.-H. Heenen, S. J. Krieger and M. S. Weiss, *Nucl. Phys. A* **443**, 39 (1985).
107. R. Rodríguez-Guzmán, P. Sarriguren, L. M. Robledo and S. Perez-Martin, *Phys. Lett. B* **691**, 202 (2010).
108. C. L. Zhang, G. H. Bhat, W. Nazarewicz, J. A. Sheikh and Y. Shi, *Phys. Rev. C* **92**, 034307 (2015).
109. J. Xiang, Z. P. Li, Z. X. Li, J. M. Yao and J. Meng, *Nucl. Phys. A* **873**, 1 (2012).
110. J. Xiang, J. M. Yao, Y. Fu, Z. H. Wang, Z. P. Li and W. H. Long, *Phys. Rev. C* **93**, 054324 (2016).
111. Z. Shi, Z. P. Li, *Phys. Rev. C* **97**, 034329 (2018).
112. L. M. Robledo, R. Rodríguez-Guzman and P. Sarriguren, *J. Phys. G: Nucl. Part. Phys.* **36**, 115104 (2009).
113. T. Nikšić, P. Ring, D. Vretenar, Y. Tian and Z. Y. Ma, *Phys. Rev. C* **81**, 054318 (2010).
114. G. H. Bhat, J. A. Sheikh, Y. Sun and U. Garg, *Phys. Rev. C* **86**, 047307 (2012).
115. A. Bohr and B. R. Mottelson, *Nuclear structure. Vol II: Nuclear deformations*, W. A. Benjamin, New York (1975).
116. B. W. Xiong and Y. Y. Wang, *At. Data Nucl. Data Tables* **125**, 193 (2019).
117. C. M. Petrache *et al.*, *Phys. Rev. C*, **86**, 044321 (2012).
118. J. Timár, Q. B. Chen, B. Kruzsicz, D. Sohler, I. Kuti, S. Q. Zhang, *et al.*, *Phys. Rev. Lett.* **122**, 062501 (2019).
119. N. Sensharma, U. Garg, Q. B. Chen, S. Frauendorf, D. P. Burdette, J. L. Cozzi, *et al.*, *Phys. Rev. Lett.* **124**, 052501 (2020).
120. H. Schnack-Petersen, *Nucl. Phys. A* **594**, 175 (1995).
121. M. Djongolov *et al.*, *Phys. Lett. B* **560**, 24 (2003).
122. S. Raman, C. W. Nestor and P. Tikkanen, *At. Data Nucl. Data Tables*, **78**, 1 (2001).
123. National Nuclear Data Center, Nuclear structure and decay data on-line library, Nudat 2.8, 2018. <https://www.nndc.bnl.gov/nudat2/>.
124. M. Rocchini, K. Hadyńska-Klęk, A. Nannini, A. Goasduff, M. Zielińska, D. Testov, *et al.*, *Phys. Rev. C* **103**, 014311 (2021).
125. M. Sugawara *et al.*, *Eur. Phys. J. A*, **16**, 409 (2003).
126. A. D. Ayangeakaa *et al.*, *Phys. Lett. B* **754**, 254 (2016).
127. Y. Toh *et al.*, *Eur. Phys. J. A*, **9**, 353 (2000).
128. A. D. Ayangeakaa, R. V. F. Janssens, S. Zhu, D. Little, J. Henderson, C. Y. Wu, *et al.*, *Phys. Rev. Lett.* **123**, 102501 (2019).
129. E. Clément, A. Gørgen, W. Korten, E. Bouchez, A. Chatillon, J.-P. Delaroche, *et al.*, *Phys. Rev. C* **75**, 054313 (2007).
130. A. E. Kavka *et al.*, *Nucl. Phys. A*, **593**, 177 (1995).
131. E. Clément *et al.*, *Phys. Rev. C* **94**, 054326 (2016).
132. M. Zielińska, Electromagnetic structure of molybdenum isotopes studied using Coulomb excitation method, Ph.D. thesis, Warsaw University, 2005.
133. M. Zielińska *et al.*, *Nucl. Phys. A* **712**, 3 (2002).
134. K. Wrzosek-Lipska *et al.*, *Phys. Rev. C* **86**, 064305 (2012).
135. J. Srebrny *et al.*, *Nucl. Phys. A* **766**, 25 (2006).
136. K. Wrzosek-Lipska *et al.*, *Acta Phys. Pol. B* **51**, 789 (2020).
137. C. Fahlander *et al.*, *Nucl. Phys. A* **485**, 327 (1988).
138. L. E. Svensson *et al.*, *Nucl. Phys. A* **584**, 547 (1995).
139. L. Morrison, K. Hadyńska-Klęk, Zs. Podolyák, D. T. Doherty, L. P. Gaffney, and L. Kaya, *et al.*, *Phys. Rev. C* **102**, 054304 (2020).
140. C. Y. Wu *et al.*, *Nucl. Phys. A* **607**, 178 (1996).
141. M. Zielinska, private communication.
142. K. Kumar, *Phys. Rev. Lett.* **28**, 249 (1972).
143. D. Cline, *Ann. Rev. Nucl. Part. Sci.* **36**, 683 (1986).

-
144. M. Bender and P.-H. Heenen, *Phys. Rev. C* **78**, 024309 (2008).
 145. T. R. Rodríguez and J. L. Egido, *Phys. Rev. C* **81** 064323 (2010).
 146. Z. C. Gao, M. Horoi and Y. S. Chen, *Phys. Rev. C* **92**, 064310 (2015).
 147. H. Euteneuer, J. Friedrich and N. Voegler, *Nucl. Phys A* **296**, 452 (1978).
 148. E. Chabanat, P. Bonche, P. Haensel, J. Meyer, R. Schaeffer, *Nucl. Phys. A* **627**, 710 (1997).
 149. A. Akmal, V. R. Pandharipande, and D. G. Ravenhall, *Phys. Rev. C* **58**, 1804 (1998).
 150. Z. H. Li and H.-J. Schulze, *Phys. Rev. C* **78**, 028801 (2008).
 151. B. Friedman and V. R. Pandharipande, *Nucl. Phys. A* **361**, 502 (1981).
 152. R. B. Wiringa, V. Fiks, and A. Fabrocini, *Phys. Rev. C* **38**, 1010 (1988).
 153. E. Fonseca, H. T. Cromartie, T.T. Pennucci, *et al.*, arXiv astro-ph 2104.00880.
 154. N. Chamel, S. Goriely, and J.M. Pearson, *Phys. Rev. C* **80**, 065804 (2009).
 155. M. B. Tsang, Y. Zhang, P. Danielewicz, M. Famiano, Zhuxia Li, W. G. Lynch, A. W. Steiner, *et al.*, *Phys. Rev. Lett.* **102**, 122701 (2009).
 156. L.-W. Chen, C. M. Ko, B.-A. Li, and J. Xu, *Phys. Rev. C* **82**, 024321 (2010).
 157. J. M. Lattimer and Y. Lim, *Astrophys. J.* **771**, 51 (2013).
 158. L. Trippa, G. Colò, and E. Vigezzi, *Phys. Rev. C* **77**, 061304(R) (2008).
 159. M. Fortin, C. Providència, Ad. R. Raduta, F. Gulminelli, J.L. Zdunik, P. Haensel, and M. Bejger, *Phys. Rev. C* **94**, 035804 (2016).
 160. T. Lesinski, K. Bennaceur, T. Duguet, and J. Meyer, *Phys. Rev. C* **74**, 044315 (2006).
 161. L. G. Cao, U. Lombardo, C. W. Shen and N.V. Giai, *Phys. Rev. C* **73**, 014313 (2006).
 162. X. R. Zhou, G. F. Burgio, U. Lombardo, H.-J. Schulze, and W. Zuo, *Phys. Rev. C* **69**, 018801 (2004).
 163. A. W. Steiner, M. Hempel, and T. Fischer, *Astrophys. J.* **774**, 17 (2013).
 164. S. Goriely, A. Bauswein, O. Just, and H.-T. Janka, *Mon. Not. Roy. Astron. Soc.* **452**, 3894 (2015).
 165. R. Ardevol-Pulpillo, H.-T. Janka, O. Just, and A. Bauswein, *Mon. Not. Roy. Astron. Soc.* **485**, 4754 (2019).
 166. T. Marketin, L. Huther, and G. Martinez-Pinedo, *Phys. Rev. C* **93**, 025805 (2016).
 167. S. Goriely, *Astron. Astrophys.* **342**, 881 (1999).
 168. S. E. Larsson, I. Ragnarsson and S. G. Nilsson, *Phys. Lett. B* **38**, 269 (1972).
 169. B. N. Lu, J. Zhao, E. G. Zhao and S. G. Zhou, *Phys. Rev. C* **89**, 014323 (2014).
 170. W. Ryssens, M. Bender, K. Bennaceur, P.-H. Heenen and J. Meyer, *Phys. Rev. C* **99**, 044315 (2019).
 171. K. Petrík and M. Kortelainen, *Phys. Rev. C* **97**, 034321 (2018).
 172. Y. Alhassid, G. F. Bertsch, L. Fang and S. Liu, *Phys. Rev. C* **72**, 064326 (2005).
 173. M.-H. Koh *et al.*, *EPJA* **52**, 3 (2016).
 174. M. Bender, K. Rutz, P.-G. Reinhard and J. A. Maruhn, *Eur. Phys. J. A* **8**, 59 (2000).

